Journal of Catalysis 389 (2020) 140–149

Contents lists available at ScienceDirect

Journal of Catalysis

journal homepage: www.elsevier.com/locate/jcat

Effects of dioxygen pressure on rates of NO_x selective catalytic reduction with NH_3 on Cu-CHA zeolites

Casey B. Jones [a,1], Ishant Khurana [a,1], Siddarth H. Krishna [a], Arthur J. Shih [a], W. Nicholas Delgass [a], Jeffrey T. Miller [a], Fabio H. Ribeiro [a], William F. Schneider [b], Rajamani Gounder [a,*]

[a] Charles D. Davidson School of Chemical Engineering, Purdue University, 480 Stadium Mall Drive, West Lafayette, IN 47907, USA
[b] Department of Chemical and Biomolecular Engineering, University of Notre Dame, 250 Nieuwland Science Hall, Notre Dame, IN 46556, USA

ARTICLE INFO

Article history:
Received 9 April 2020
Revised 28 April 2020
Accepted 16 May 2020
Available online 28 May 2020

Keywords:
Cu-CHA zeolites
NO_x selective catalytic reduction
Oxidation-limited kinetics
Reduction-limited kinetics
In operando spectroscopy

ABSTRACT

At low temperatures (<523 K), the selective catalytic reduction (SCR) of NO with NH_3 on Cu-exchanged zeolites occurs via elementary steps catalyzed by NH_3-solvated Cu ions, which are reactive intermediates in a Cu^{II}/Cu^{I} redox cycle. SCR rates are typically measured under "standard" reaction conditions, in which O_2 is the oxidant and present at partial pressures (~10 kPa O_2) that cause both single-site Cu^{II} reduction and dual-site Cu^{I} oxidation to behave as kinetically relevant steps. As a result, "standard" SCR rates (per g) transition from a second-order to a first-order dependence on isolated Cu content (per g) among Cu-CHA zeolites with increasing Cu content and thus spatial density (Si/Al = 15, Cu/Al = 0.08–0.37), as dual-site Cu^{I} oxidation steps limit SCR rates to lesser extents. On a given Cu-CHA catalyst, SCR rates (per Cu, 473 K) show a Langmuirian dependence on dioxygen pressure when varied widely (0–60 kPa O_2), enabling the isolation of first-order or zero-order kinetic regimes with respect to O_2. These kinetic regimes respectively correspond to limiting conditions in which either Cu^{I} oxidation or Cu^{II} reduction becomes the dominant kinetically relevant step, consistent with *in operando* X-ray absorption spectra. First-order rate constants (per Cu) increase approximately linearly with Cu density, reflecting the dual-site requirement of O_2-assisted Cu^{I}-oxidation steps. Zero-order rate constants (per Cu) increase more gradually with Cu density, in part reflecting the increasing fraction of isolated Cu ions that are able to form binuclear intermediates and thus participate in SCR turnovers. Combining steady-state and transient kinetic data with *in operando* spectra provides a methodology to quantitatively describe the rate dependences of SCR reduction and oxidation processes on Cu-zeolite properties such as Cu ion density as shown here, and others including the zeolite framework topology and its density and distribution of Al atoms.

1. Introduction

Selective catalytic reduction (SCR) with ammonia is a strategy used to abate nitrogen oxide (NO_x, x = 1,2) emissions from diesel and lean-burn engines, and was implemented commercially about a decade ago with the advent of Cu-CHA zeolite catalysts that have sufficient hydrothermal stability to withstand the harsh environments encountered in automotive exhaust applications [1–3]. Typical protocols to evaluate catalysts for practical application have focused on the measurement of NO_x conversion profiles as a function of temperature [4], including identifying the onset of the rapid increase in NO_x conversion with increasing temperature (i.e., "light-off") observed at low temperatures (<473 K) and the decrease in NO_x conversion with increasing temperature (i.e., "seagull"-shaped dip) observed at intermediate temperatures (523–623 K) [5–8]. Such macroscopic observations are manifestations of the underlying kinetic and mechanistic details of the SCR reaction on Cu-zeolites; they depend on the microscopic details of catalyst composition and active site arrangement. On Cu-CHA zeolites, these details include the number and spatial distribution of Cu cations exchanged at anionic framework sites introduced by Al substitution, and the fraction of Cu present nominally as monovalent $[Cu^{II}OH]^{+}$ (i.e., ZCuOH) and divalent Cu^{II} (i.e., Z_2Cu) sites that respectively charge-compensate one and two framework Al centers [4,9–11].

The stoichiometry of the SCR reaction using molecular oxygen as the oxidant, which is also referred to as the "standard" SCR reaction, is:

* Corresponding author.
E-mail address: rgounder@purdue.edu (R. Gounder).
[1] C. B. J. and I. K. contributed equally to this work.

https://doi.org/10.1016/j.jcat.2020.05.022
0021-9517/

$$4NO + 4NH_3 + O_2 \rightarrow 4N_2 + 6H_2O \quad (1)$$

Rates of "standard" SCR are typically measured at ambient pressures with NO and NH_3 present in equimolar quantities (e.g., 0.03 kPa each), and O_2 is present in large stoichiometric excess (e.g., 10 kPa), to resemble the concentrations present in lean-burn exhaust. The observed coexistence of both Cu^I and Cu^{II} species under "standard" SCR reaction conditions, and the sensitivity of their proportions to catalyst composition and structure and to the specific reaction conditions used, points to a mechanism involving a redox cycle between these two Cu states [12]. At temperatures below ~ 523 K and under SCR-relevant conditions, exchanged Cu ions in Cu-CHA zeolites are fully solvated by NH_3 ligands, as evidenced by phase diagrams constructed from first-principles thermodynamic analyses of density functional theory (DFT)-based free energies of Cu-ligand complexes [9], by *in situ* X-ray emission spectra (XES) that show Cu-N coordination in their oxidized (Cu^{II}) and reduced (Cu^I) states [7,13], and by *in situ* X-ray absorption near edge structure (XANES) and extended X-ray absorption fine structure (EXAFS) spectra of their oxidized and reduced states that are indistinguishable from those for four-fold and two-fold Cu-amine coordination complexes [9,14], respectively. The coordination of Cu ions to ammonia ligands and not to zeolite framework oxygen atoms is further evidenced by the absence of second-shell Cu-T atom (T = Si, Al) scattering in EXAFS spectra collected *in operando* [9] and the absence of perturbed zeolite framework T-O-T vibrations in diffuse reflectance IR (DRIFTS) spectra collected *in situ* [15]. Thus, during low temperature NO_x SCR on Cu-CHA zeolites, ammonia-solvated Cu ions are present as cationic complexes that are ionically bonded to anionic zeolite framework centers.

The preponderance of evidence is consistent with a reduction half-cycle that consumes both NO and NH_3, which proceeds by NO attack on Cu^{II}-amine complexes to form nitrosamine (H_2NNO)-like intermediates that decompose to yield N_2, H_2O, Cu^I-amine complexes, and an excess proton [16]. The excess proton formed upon reduction of Z_2Cu sites resides on the zeolite lattice at framework oxygen adjacent to an Al site, while that formed upon reduction of ZCuOH is rejected as H_2O [9]. Evidence for the reduction mechanism of mononuclear Cu^{II}-amine complexes includes DFT calculations of plausible Cu^{II} reduction pathways [9,14,16,17], transient XAS [14,16] and TPR measurements [18] that detect complete and stoichiometric reduction of Cu^{II} to Cu^I only when both NO and NH_3 are present, and NH_3 titrations that quantify the zeolitic H^+ sites formed upon reduction of Z_2Cu sites [9]. The details of the oxidation half-cycle are less well understood [6,14,19,20], although O_2 must be consumed to balance stoichiometry. The oxidation of pairs of Cu^I complexes with O_2 is well-known in the homogeneous Cu literature [21–23]. Mononuclear $Cu^I(NH_3)_2$ complexes can react with O_2 to form NH_3-solvated binuclear Cu^{II} di-oxo complexes (e.g., $(NH_3)_2Cu^{II}(O_2)Cu^{II}(NH_3)_2$) [6,19], consistent with DFT calculations of plausible dual-site Cu^I oxidation pathways with O_2 [6,19,24,25] and with EXAFS spectra of Cu-CHA zeolites after their NH_3-solvated Cu^I ions are oxidized by O_2 that show second-shell Cu-Cu scattering at distances characteristic of binuclear Cu^{II} di-oxo complexes [19]. NH_3-solvated binuclear Cu^{II} di-oxo complexes can be reduced to two Cu^I sites while consuming two equivalents of NO and NH_3 to balance stoichiometry [19], via a sequence of elementary steps whose precise details have yet to be clarified.

Under low temperature "standard" SCR conditions, reaction rates on Cu-CHA (per mass or per pore volume catalyst) increase monotonically with the spatial density of isolated Cu ions (per mass or per pore volume catalyst), transitioning from a second-order dependence on Cu density in the dilute Cu limit to a first-order dependence on Cu density at higher Cu densities [9,19,26,27]. *In operando* X-ray absorption spectra (XAS) provide direct evidence that $Cu^I(NH_3)_2$ is the most abundant reactive intermediate (MARI) at low Cu densities under "standard" SCR conditions [19], implying that $Cu^I(NH_3)_2$ oxidation with O_2 is the dominant kinetically-relevant process in the kinetic regime characterized by SCR rates that show a second-order dependence on Cu density. This interpretation is consistent with transient XAS experiments performed to measure O_2-assisted oxidation rates of $Cu^I(NH_3)_2$ complexes in Cu-CHA, which are best described by rate equations that are second-order in $Cu^I(NH_3)_2$ concentration [19]. Transient XAS experiments were also used to quantify the fraction of $Cu^I(NH_3)_2$ complexes that were oxidized by O_2 in the asymptotic limit of long reaction times, and this fraction was found to increase monotonically with Cu spatial density [19]. These findings indicate that O_2-assisted oxidation steps require two $Cu^I(NH_3)_2$ complexes, nominally isolated from one another, to co-locate within a single CHA cage to form a binuclear Cu^{II} di-oxo complex. DFT calculations indicate that transport of $Cu^I(NH_3)_2$ through an 8-MR window into an adjacent CHA cage that already contains a $Cu^I(NH_3)_2$ complex occurs with lower barriers (~35 kJ mol^{-1}) [19] than the measured range of apparent SCR activation barriers (~40–80 kJ mol^{-1}) [6,14,19], and that subsequent reaction steps to form binuclear Cu^{II} di-oxo complexes are even more facile [19,24,28].

Quantitative measurements that distinguish between the number of Cu sites that participate in SCR redox cycles, and the kinetics of reduction and oxidation processes catalyzed by such Cu sites, are difficult to extract from SCR rates measured under "standard" conditions that invariably convolute the kinetic contributions of both the oxidation and reduction half-cycles [12,14,16,19,29]. Here, we interrogate the catalytic function of Cu-CHA zeolites under reaction conditions perturbed far from those typical of "standard" SCR, in order to isolate either Cu^{II} reduction or Cu^I oxidation as the dominant kinetically-relevant process. Given that O_2 is only involved as a reactant in the oxidation half-cycle, we hypothesize that dual-site Cu^I oxidation becomes the dominant kinetically-relevant step at dilute O_2 pressures and becomes kinetically-irrelevant at higher O_2 pressures. We use *in operando* XAS measurements to quantify the prevalent Cu^{II} and Cu^I fractions as a function of reaction conditions and Cu density. Apparent Cu^{II} reduction and Cu^I oxidation rate constants are determined from regression of rate data to an empirical model that captures the observed Langmuirian dependence of SCR rates on O_2 pressure, which allows extracting kinetic parameters that describe the effects of Cu ion spatial density on SCR oxidation and reduction processes.

2. Experimental methods

2.1. Zeolite synthesis

The parent CHA zeolites (SSZ-13, Si/Al = 15) were synthesized using previously reported procedures [9]. Briefly, a molar ratio of 1 SiO_2/ 0.033 Al_2O_3/ 0.25 TMAdaOH/ 0.25 Na_2O/ 44 H_2O was used in the synthesis solution. An aqueous TMAdaOH solution (25 wt%, Sachem) was first added to deionized H_2O (18.2 MΩ•cm) in a perfluoroalkoxy alkane jar (PFA, Savillex Corp.), followed by stirring the solution under ambient conditions for 0.25 h. Next, aluminum hydroxide ($Al(OH)_3$, grade 0325, SPI Pharma) was added to the aqueous TMAdaOH solution. Then, a 5 M NaOH solution (16.7 wt % NaOH in deionized water; NaOH pellets 98 wt%, Alfa Aesar) was added dropwise to the solution and stirred under ambient conditions for 0.25 h. Lastly, fumed silica (SiO_2, 99 wt%, Cabot) was added, and the mixture was stirred for 2 h under ambient conditions. The obtained synthesis solution was then transferred to a 45 mL Teflon-lined stainless-steel autoclave (Parr) and placed in

a forced convection oven (Yamato DKN-402C) at 433 K and rotated at 40 RPM for 6 days.

Cu-form zeolites were prepared via aqueous-phase Cu ion exchange of H-form zeolites using a $Cu^{II}(NO_3)_2$ solution (0.001–0.1 M, 100 $cm^3\ g_{cat}^{-1}$; 99.999 wt%, Sigma-Aldrich) for 4 h and 300 RPM at ambient conditions, during which dropwise addition of 1.0 M NH_4OH (Sigma-Aldrich) was used to control the pH at 4.9 ± 0.1, as reported previously [9]. The resulting Cu-form zeolites were recovered by centrifugation and washed six times with deionized water (70 $cm^3\ g_{cat}^{-1}$ per wash), dried in an oven at 373 K, and then treated in flowing dry air (1.67 $cm^3\ s^{-1}\ g_{cat}^{-1}$; Zero Grade, Indiana Oxygen) to 773 K (0.0167 K s^{-1}) for 4 h.

2.2. Characterization of H-form and Cu-form CHA zeolites

X-ray diffraction (XRD) patterns (Fig. S1, SI) of the synthesized CHA samples were used to confirm crystal topology, and were collected using a Rigaku SmartLab X-ray diffractometer equipped with a Cu Kα X-ray source (40 kV, 44 mA) from 4 to 40° 2θ with a scan rate of 0.00833° s^{-1} and a step size of 0.01°. The micropore volumes of the H-CHA samples were calculated from Ar adsorption isotherms measured at 87 K (Fig. S2, SI) using a Micromeritics ASAP 2020 Surface Area and Porosity Analyzer; micropore volumes (0.20 $cm^3\ g^{-1}$) were consistent with previously reported values for the CHA framework [9].

Elemental analysis of the Cu and H-form zeolites (Si, Al, Cu) was performed using atomic absorption spectroscopy (AAS) on a Perkin-Elmer AAnalyst 300. Samples were digested for AAS by adding 0.01 g of zeolite to 2 g of hydrofluoric acid (48 wt%, Sigma Aldrich) and allowing to sit at ambient conditions for 72 h, followed by dilution in 50 g of water (18 MΩ•cm). *Warning: when using HF acid, always use adequate personal protective equipment and ventilation*. The absorbances of Al and Si were measured using a reducing nitrous oxide-acetylene flame at wavelengths of 309.3 and 251.6 nm, respectively. The absorbance of Cu was measured using an oxidizing air-acetylene flame at a wavelength of 324.8 nm. Absorbances were converted into concentrations using calibration solutions of known concentrations for each element.

The total number of H^+ sites on H-form zeolites and the residual number of H^+ sites on Cu-form zeolites were quantified by NH_3 titration (Table S1, SI) after zeolite samples were treated in an oxidative environment (10 kPa O_2, balance N_2, 773 K, 4 h) using previously reported methods [30,31]. Zeolite samples (0.03–0.05 g) were first saturated with gas-phase NH_3 (0.050 kPa in He, Indiana Oxygen) at 433 K for 2 h (0.05 kPa NH_3, balance He, 5.8 $cm^3\ s^{-1}$), followed by selective removal of Lewis acid-bound and physisorbed NH_3 by treatment in a flowing wet helium stream at 433 K for 8 h (2.5–3.0 kPa H_2O in balance He, 5.8 $cm^3\ s^{-1}$), in order to selectively retain surface NH_4^+ species [31]. NH_3 was then desorbed in a subsequent temperature-programmed desorption (TPD) in flowing He (UHP, 99.999%, Indiana Oxygen, 5.8 $cm^3\ s^{-1}$) to 823 K (0.083 K s^{-1}), and quantified using on-board calibrations in a gas-phase FTIR spectrometer (MKS Multigas™ 2030). The speciation of Cu between sites that are nominally either Cu^{II} or $Cu^{II}OH$ was determined from a site balance that considered total Cu content, the difference in H^+ sites titrated on H-form and Cu-form samples, and the expected 2:1 and 1:1 H^+:Cu exchange stoichiometry, respectively (Table S1, SI).

2.3. In operando and transient X-ray absorption spectroscopic characterization of Cu-CHA

X-ray absorption spectroscopy (XAS) experiments were carried out at the Advanced Photon Source (APS) at Argonne National Laboratory on the insertion device (ID) beam line of the Materials Research Collaborative Access Team (MRCAT, Sector 10) [32]. A cryogenically cooled double-crystal Si(111) monochromator with an uncoated glass mirror was used to minimize the presence of harmonics. Spectra were recorded in transmission mode with the ionization chambers optimized for the maximum current with a linear response (~10^{10} photons s^{-1}) using gas mixtures to give 10% absorption in the incident X-ray detector and 70% absorption in the transmission X-ray detector. Calibration of the Cu K-edge to 8979 eV was performed by simultaneously collecting a Cu metal foil spectrum while collecting sample spectra. Spectra were collected under isothermal conditions and normalized using a first-order polynomial in the pre-edge region and a third-order polynomial in the post-edge region. Linear combination fitting of the XANES spectra was performed using standards for Cu^I (Cu-CHA zeolite reduced in NO and NH_3 at 473 K) and Cu^{II} (Cu-CHA zeolite oxidized in 20 kPa O_2 to 673 K, spectra measured at 473 K) [16] to determine the fractions of Cu^I and Cu^{II} species present.

In operando experiments were performed in a glassy carbon tube reactor described previously [12], in which steady-state SCR rate measurements (reaction conditions given in Section 2.4) were collected simultaneously with XAS spectra to verify that rates were identical to those measured in separate differential plug-flow reactor experiments. Multiple spectra were taken to confirm the absence of beam damage to the sample or any other time-dependent changes. Transient NO and NH_3 reduction experiments were carried out by first oxidizing the sample in flowing O_2 (20 kPa O_2 in balance N_2, Airgas, 13.3 $cm^3\ s^{-1}$) at 673 K for 0.5 h, after which the sample was cooled to 473 K. After purging for 0.08 h in flowing N_2 (13.3 $cm^3\ s^{-1}$, Airgas), flowing NH_3 (0.03 kPa in balance N_2, Airgas, 13.3 $cm^3\ s^{-1}$) was introduced to the sample. Shortly thereafter (approximately 0.01–0.08 h), flowing NO was added to the gas stream (0.03 kPa NO, 0.03 kPa NH_3, Airgas, balance N_2, 13.3 $cm^3\ s^{-1}$) concurrently with the start of collecting XAS spectra. Transient O_2 oxidation experiments were then carried out, starting with the catalyst in the state at the end of the NO and NH_3 reduction. After purging in flowing N_2 (13.3 $cm^3\ s^{-1}$) for 0.08 h, flowing O_2 (20 kPa in N_2, Airgas, 13.3 $cm^3\ s^{-1}$) was introduced concurrently with the start of collecting XAS spectra. For both of the reduction and oxidation experiments, spectra were collected until changes were no longer detectable.

2.4. Measurement of standard SCR kinetics under differential conditions

Selective catalytic reduction (SCR) kinetics were measured using a bench-top tubular quartz reactor system described previously [33]. Zeolite samples were sieved to obtain aggregate particle sizes between 125 and 250 μm in diameter. A bed height of approximately 1 cm was obtained by dilution with silica gel (Davisil, 250–500 μm in diameter). NO conversions were kept below 20% for all steady-state kinetic measurements to ensure that the entire catalyst bed was exposed to approximately the same gas concentrations, using a reactant gas mixture of 0.03 kPa NO (3.5% NO/Ar, Praxair), 0.03 kPa NH_3 (3.0% NH_3/Ar, Praxair), 7 kPa CO_2 (liquid, Indiana Oxygen), 1–60 kPa O_2 (99.5%, Indiana Oxygen), 1 kPa H_2O (deionized, 18.2 MΩ•cm, introduced through a 24" Perma Pure MH Nafion™ Series Humidifier), and balance N_2 (boil-off from a liquid N_2 dewar) at 473 K and ambient total pressure. The balance N_2 was composed of two independent streams, one which passed through the humidifier and was used as a carrier to maintain gas-phase water partial pressures at 1 kPa ("wet" N_2) and the other which was used as a diluent carrier for the other gas-phase reactants ("dry" N_2). The gas mixing pattern was designed such that the 3.5% NO/Ar stream was pre-diluted by the "wet" N_2 carrier stream and CO_2 prior to mixing with the "dry" N_2 and O_2 stream, in order to mitigate background NO_2 formation that occurs upon mixing of concentrated NO and O_2 streams. The

total gas flow rate was 16.7–33.3 $cm^3\ s^{-1}$ (at ambient temperature and pressure) and selected to maintain differential NO conversion. Outlet NO, NO_2, NH_3, CO_2, and H_2O concentrations were measured every 0.95 s using on-board gas calibrations on a gas-phase Fourier Transform Infrared (FTIR) spectrometer (MKS Multigas™ 2030).

The rate of NO consumption was calculated according to:

$$-r_{NO} = \frac{(y_{NO,in} - y_{NO,out})}{10^6} \frac{P\dot{V}_{total}}{RT} \quad (2)$$

where y is the volume fraction of NO in ppm, $\dot{V}_{total}$ is the total volumetric flow rate, P is the ambient pressure, T is the ambient temperature, and R is the gas constant. The SCR rate was determined by correcting the overall rate of NO consumption in each experiment for contributions to NO consumption resulting from "fast" SCR reactions with NO_2, present both as an impurity in NO reactant cylinders and formed as a product from homogeneous NO oxidation reactions within the reactor unit (details in Section S.3, SI). These methods were validated by measuring identical SCR rates independently in two different reactor units, with different rates of background NO_2 formation and, in turn, contributions from "fast" SCR reactions (details in Section S.3, SI). Measured SCR rates were independent of space velocity (Fig. S6, SI) and thus insensitive to external transport phenomena (details in Section S.4, SI) [9,33,34]. Measured SCR rates were also found not to be corrupted by intracrystallite transport phenomena according to the Weisz-Prater criterion (details in Section S.4, SI) [35]. In addition, SCR rates were independent of H_2O (0.2–4 kPa) [19,36] and CO_2 (0–16 kPa) [33,36] pressures as reported in our prior work.

Apparent NO and NH_3 reaction orders on Cu-CHA zeolites were measured at three different O_2 pressures (1, 10, 60 kPa O_2) at 473 K, holding the concentration of other gases fixed (1 kPa H_2O, 7 kPa CO_2, balance N_2, 0.030 kPa NO or NH_3) while maintaining differential conversion. The NO concentration was varied between 0.015 and 0.060 kPa for the NO reaction order measurement, while the NH_3 concentration was varied between 0.015 and 0.090 kPa for the NH_3 reaction order measurement (all partial pressure changes were made in random order). Similarly, the apparent reaction orders in O_2 in the low, "standard", and high O_2 pressure limits were measured by varying dioxygen pressure from 1 to 4 kPa (a range of 2–5 kPa was used for Cu-CHA-0.078, Cu-CHA-0.084, and Cu-CHA-0.10; details in Section S.5, SI), 5–15 kPa and 40–60 kPa, respectively, while maintaining differential conversion and holding other gas pressures constant (0.030 kPa NO, 0.030 kPa NH_3, 1 kPa H_2O, 7 kPa CO_2 in balance N_2 at 473 K). The logarithm of SCR reaction rates was plotted against the logarithm of reactant concentration and regressed to a linear function, whose slope was taken as the apparent reaction order (Figs. S9-S11, SI).

3. Results and discussion

3.1. Both Cu^I oxidation and Cu^{II} reduction steps are kinetically relevant during "standard" SCR

In order to study the effects of Cu ion density on the Cu^I oxidation and Cu^{II} reduction processes that occur during steady-state SCR turnover, a series of Cu-CHA samples was prepared by starting with H-form zeolites of fixed framework Al content (Si/Al = 15) and performing Cu ion exchange to varying extents (Cu/Al = 0.08–0.37, Table 1; additional characterization data reported in Table S1, SI and in our prior study [19]). Cu-CHA samples are denoted as Cu-CHA-X, where X denotes the mean Cu volumetric density (number of Cu atoms per 1000 $Å^3$) assuming a homogeneous Cu distribution throughout the crystallite volume (details in our prior study [19]). Mean Cu volumetric densities vary from 0.078 to 0.35 Cu atoms per 10^3 $Å^3$ from the least to most heavily Cu-exchanged samples, respectively corresponding to approximately one Cu ion per seventeen to four CHA cages (Table 1).

SCR rates (per 10^3 $Å^3$, 473 K) were measured at 1, 10 and 60 kPa O_2 on these Cu-CHA samples and are plotted as a function of Cu volumetric density (per 10^3 $Å^3$) in Fig. 1a. The corresponding fraction of total Cu (Cu_{tot}) present in the Cu^{II} state (Cu^{II}/Cu_{tot}), as measured *in operando* by XAS, at these three O_2 pressures is shown in Fig. 1b. SCR rates measured at 10 kPa O_2 (Fig. 1a, circles), which are representative of "standard" SCR conditions, increase with a second-order dependence on Cu density at low values of Cu density (<0.2 Cu per 10^3 $Å^3$) and gradually transition to increasing with a first-order dependence on Cu density at high values of Cu density (>0.3 Cu per 10^3 $Å^3$), consistent with prior reports [19,26]. At dilute values of Cu density (<0.1 Cu per 10^3 $Å^3$), *in operando* XAS spectra reveal that $Cu^I(NH_3)_2$ is the MARI (<0.30 Cu^{II}/Cu_{tot}, Fig. 1b) under "standard" SCR conditions. These data indicate that Cu^I oxidation with O_2 becomes the dominant kinetically relevant step when measured SCR rates show a second-order dependence on Cu density, consistent with mechanistic proposals for the involvement of two $Cu^I(NH_3)_2$ complexes in O_2-assisted oxidation steps [19]. With increasing Cu density, the fraction of Cu^{II} present during steady-state SCR at 10 kPa O_2 increases (Fig. 1b, circles) as single-site Cu^{II} reduction processes increase in kinetic relevance, as also reported previously [19].

Apparent reaction orders in O_2 measured in pressure ranges characteristic of the low (1–5 kPa O_2), "standard" (5–15 kPa O_2) and high (40–60 kPa O_2) pressure regimes are shown in Table 2. With increasing Cu density, apparent reaction orders in O_2 at "standard" SCR conditions decrease systematically from 0.8 to 0.3 (Table 2), as single-site Cu^{II} reduction increases in kinetic relevance. These data reveal that both Cu^{II} reduction and Cu^I oxidation are kinetically relevant steps when low-temperature SCR rates (473 K) are measured under "standard" reaction conditions (10 kPa O_2), for Cu-CHA composition ranges similar to those typically used in practice (Si/Al ~ 15, Cu/Al ~ 0.5) [37]. These data also indicate that measured SCR rates become more sensitive to the kinetics of Cu^I oxidation steps as the Cu density becomes more dilute, given the dual-site requirements of O_2-assisted oxidation of NH_3-solvated Cu^I ions and the single-site requirements of NO + NH_3-assisted reduction of NH_3-solvated Cu^{II} ions.

The net rates of Cu^{II} reduction and Cu^I oxidation steps in the SCR redox cycle must be equal during steady-state catalytic turnover; yet, the rates of such steps depend on the apparent rate constants and the pressures of reactants involved in them. Current mechanistic proposals involve dioxygen as a reactant only in the Cu^I oxidation step, suggesting that varying the O_2 pressure should change the rates of Cu^I oxidation processes, but not of Cu^{II} reduction processes. In turn, varying the O_2 pressure should change the extent to which each step limits the rates of the overall SCR redox cycle, and lower O_2 pressures should cause Cu^I oxidation rates to become increasingly rate-limiting. Insights into the kinetically-relevant processes at varying O_2 pressure are also relevant to practical SCR implementation, as transient excursions to low O_2 pressures (e.g., 2 kPa O_2) occur during operation of diesel vehicles (e.g., rapid acceleration), and have been observed to cause decreases in NO_x conversion [38]. In the range of Cu density values studied, SCR rates (per 10^3 $Å^3$, 473 K) on Cu-CHA are systematically higher at 60 kPa O_2 than at 10 kPa O_2 (Fig. 1a), and the fraction of Cu^I present *in operando* is systematically lower at 60 kPa O_2 than at 10 kPa O_2 (Fig. 1b). Conversely, SCR rates (per 10^3 $Å^3$, 473 K) are systematically lower at 1 kPa O_2 than at 10 kPa O_2 (Fig. 1a), and the fraction of Cu^I present *in operando* is systematically higher at 1 kPa O_2 than at 10 kPa O_2 (Fig. 1b). Additionally, apparent reaction orders in O_2 approach unity at low pressures (<5 kPa O_2), decrease systematically with increasing pressure, and approach zero at high pressures (>50 kPa O_2), as listed in Table 2 (additional details in Section S.5,

Table 1
Characterization data of the Cu-CHA samples studied.

Cu-CHA-X	Cu/Al	Cu wt%	Cu volumetric density (per 10^3 Å^3)	Cu per CHA cage	Number of cages per Cu
Cu-CHA-0.078	0.08	0.55	0.078	0.06	16.7
Cu-CHA-0.084	0.09	0.59	0.084	0.06	15.4
Cu-CHA-0.10	0.10	0.69	0.10	0.08	13.3
Cu-CHA-0.17	0.18	1.21	0.17	0.13	7.5
Cu-CHA-0.23	0.24	1.60	0.23	0.18	5.7
Cu-CHA-0.29	0.31	2.04	0.29	0.22	4.5
Cu-CHA-0.31	0.33	2.16	0.31	0.24	4.2
Cu-CHA-0.35	0.37	2.47	0.35	0.27	3.7

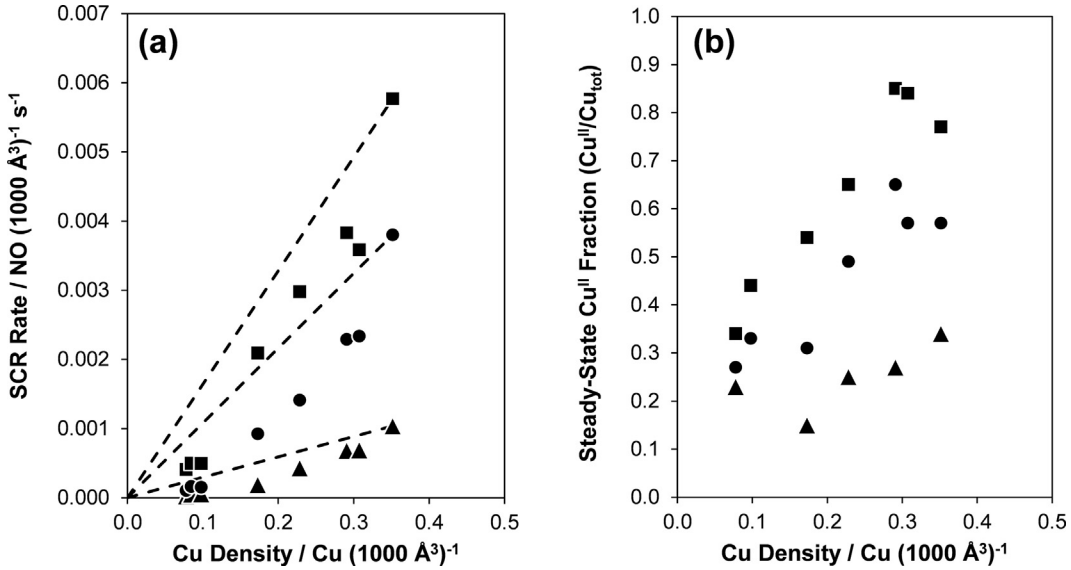

Fig. 1. (a) SCR rates (per 10^3 Å^3, 473 K) measured on Cu-CHA-X samples at 1 (▲), 10 (●), and 60 kPa (■) O_2 (other reaction conditions: 0.030 kPa NO, 0.030 kPa NH_3, 7 kPa CO_2, 1 kPa H_2O, balance N_2). Dashed lines are drawn through the origin and the rate on Cu-CHA-0.35 for each data series to guide the eye, illustrating that SCR rates deviate from a first-order dependence at dilute Cu density. (b) Steady-state Cu^{II} fraction (Cu^{II}/Cu_{tot}) at 1 (▲), 10 (●), and 60 kPa (■) O_2 measured *in operando* by XAS as a function of Cu density on Cu-CHA-X samples.

Table 2
Apparent O_2 reaction orders measured on Cu-CHA samples near low (1 kPa O_2), "standard" (10 kPa O_2) and high (60 kPa O_2) dioxygen pressures.

Sample	Apparent O_2 Order[a]		
	1 kPa O_2	*10 kPa O_2*	*60 kPa O_2*
Cu-CHA-0.078	0.6	0.8	0.4
Cu-CHA-0.084	1.0	0.7	0.6
Cu-CHA-0.10	0.9[b]	0.7	0.4
Cu-CHA-0.17	0.8	0.6	0.2
Cu-CHA-0.23	0.7	0.5	0.2
Cu-CHA-0.29	0.5	0.4	0.0
Cu-CHA-0.31	0.5	0.3	0.0
Cu-CHA-0.35	0.5	0.3	0.1

[a] Other conditions: 0.030 kPa NO, 0.030 kPa NH_3, 7 kPa CO_2, 1 kPa H_2O and balance N_2 at 473 K. Uncertainties are ± 0.1, unless otherwise noted.
[b] Uncertainty is ± 0.3.

SI). These trends are consistent with the preferential decrease in intrinsic Cu^I oxidation rates relative to intrinsic Cu^{II} reduction rates at lower O_2 pressures.

These data serve as yet another reminder that the extent to which Cu^I oxidation steps limit SCR rates depends both on the sample composition and the reaction conditions used, given the different kinetic and active site requirements of Cu^I oxidation and Cu^{II} reduction processes in the SCR redox cycle. The kinetic relevance of Cu^I oxidation steps increases both with decreasing Cu ion density and with decreasing O_2 pressure. Yet, even at low but fixed O_2 pressure (1 kPa), SCR rates are not solely limited by the rates of Cu^I oxidation steps, as evident by the finite Cu^{II} fractions (0.15–0.35) quantified *in operando* by XANES. Thus, we next systematically investigate the steady-state catalytic behavior of Cu-CHA zeolites under widely varying O_2 pressures, in order to isolate limiting kinetic behavior that allows deconvoluting the influence of Cu^I oxidation and Cu^{II} reduction steps on overall rates of SCR redox cycles.

3.2. Effects of O_2 pressure on SCR rates and the Cu^{II}/Cu^I redox balance

SCR rates (per Cu_{tot}, 473 K) measured on a representative Cu-CHA sample (Cu-CHA-0.23) as a function of O_2 pressure are shown in Fig. 2a. SCR rates (per Cu_{tot}) show a Langmuirian dependence on O_2 pressure when varied over a wide range (1–60 kPa O_2), according to the following empirical rate expression:

$$\frac{-r_{NO}}{[Cu_{tot}]} = \frac{k_{first}k_{zero}P_{O_2}}{k_{zero} + k_{first}P_{O_2}} \quad (3)$$

where k_{first} is the apparent rate constant in the limiting kinetic regime that is first-order in O_2 pressure, and k_{zero} is the apparent rate constant in the limiting kinetic regime that is zero-order in O_2 pressure (additional details of the kinetic fitting in Section S.5, SI). The corresponding steady-state fraction of Cu present in the Cu^{II} state (Cu^{II}/Cu_{tot}), measured *in operando* by XANES, is shown on the secondary ordinate in Fig. 2a (*in operando* XANES spectra of Cu-CHA-0.23 shown in Fig. S12, SI). In the first-order dioxygen pressure limit, Cu ions are predominantly in their Cu^I state (Cu^{II}/Cu_{tot} = 0.25,

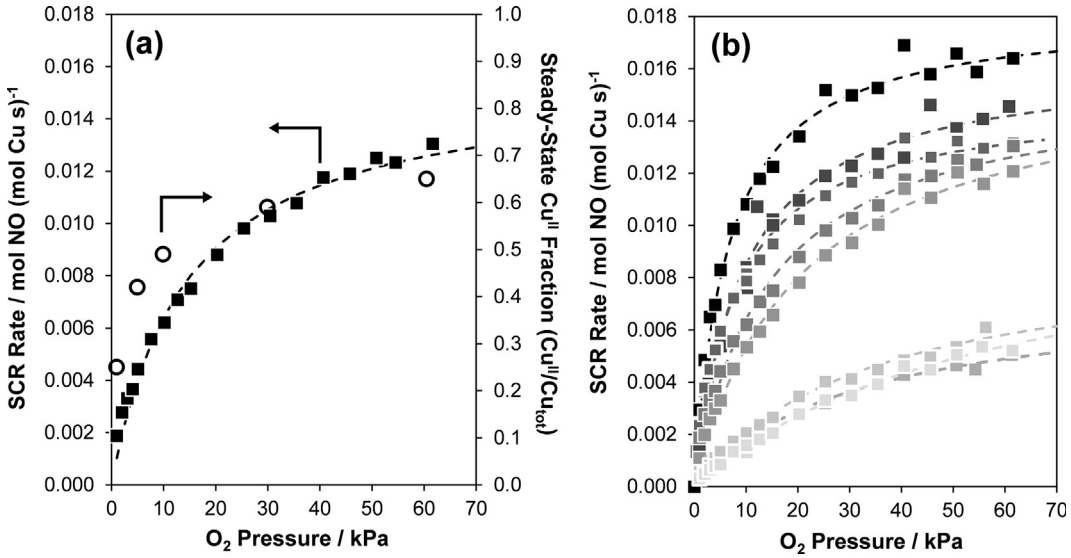

Fig. 2. (a) Steady-state SCR rate (per Cu_{tot}, 473 K, ■) and Cu^{II} fraction (Cu^{II}/Cu_{tot}) (○) as a function of O_2 pressure on Cu-CHA-0.23; dashed line represents the best-fit regressions of rates to Eq. (3). (b) Steady-state SCR rate (per Cu, 473 K) as a function of O_2 pressure on all Cu-CHA-X samples (X increases with light-to-dark shading); dashed lines represent best-fit regressions of rates to Eq. (3).

Fig. 2a), consistent with dual-site oxidation of $Cu^{I}(NH_3)_2$ with O_2 becoming the dominant kinetically relevant step in this regime. The steady-state Cu^{II} fraction increases systematically with increasing O_2 pressure (Fig. 2a), as Cu^{II} reduction steps increase in kinetic relevance. These findings are also consistent with a recent report by Liu et al. that the steady-state Cu^{II} fraction increased systematically with O_2 pressures (0–10 kPa; other conditions: 473 K, 0.1 kPa NO, 0.1 kPa NH_3, balance He) for Cu-CHA compositions (Si/Al = 15, Cu/Al = 0.03 and 0.29) similar to those studied here [39].

Importantly, the steady-state Cu^{II} fraction asymptotically approaches a non-unity value (Cu^{II}/Cu_{tot} = 0.65, Fig. 2a) under conditions (60 kPa O_2) that nearly approach the zero-order dioxygen pressure limit (apparent O_2 order = 0.2). This limiting condition should correspond to a kinetic regime in which Cu^{II} reduction becomes the sole kinetically-relevant step, and should have resulted in Cu^{II} as the sole MARI (Cu^{II}/Cu_{tot} = 1) if every Cu ion were able to participate in the SCR redox cycle. The presence of a finite fraction of Cu^{I} in the zero-order dioxygen pressure limit would therefore suggest that some Cu^{I} ions are unable to participate in SCR turnovers, which can be rationalized from data reported in our prior study [19]. Reduction of Cu-CHA samples to their $Cu^{I}(NH_3)_2$ states in flowing NO and NH_3 (473 K), followed by exposure to flowing O_2 (473 K) resulted in the transient oxidation of only a fraction of the $Cu^{I}(NH_3)_2$ species present [19]. A recalcitrant fraction of $Cu^{I}(NH_3)_2$ remained unoxidized at long O_2 exposure times, either because they were physically or functionally isolated from other $Cu^{I}(NH_3)_2$ complexes and thus unable to oxidize via the dual-site mechanism to form a binuclear Cu^{II} di-oxo intermediate. In turn, any such recalcitrant $Cu^{I}(NH_3)_2$ complexes would not contribute to measured SCR rates, and thus persist as the Cu^{I} fraction measured on Cu-CHA zeolites at high O_2 pressures when SCR rates are limited predominantly by Cu^{II} reduction steps.

SCR rates (per Cu, 473 K) as a function of O_2 pressure are shown in Fig. 2b for Cu-CHA samples of increasing Cu volumetric density (Table 1). For each Cu-CHA sample, SCR rates show a Langmuirian dependence on O_2 pressure, according to Equation (3). In the entire range of Cu density values studied (0.078–0.35 Cu per 1000 Å^3), SCR rates (per Cu_{tot}) at a fixed O_2 pressure increase systematically with Cu volumetric density (Fig. 2b). These trends include rates that are measured at low (1 kPa O_2) and high (60 kPa O_2) dioxygen pressures, which begin to approach the first-order and zero-order kinetic regimes, albeit to different extents on Cu-CHA samples of different Cu density (Table 2). The first-order kinetic regime in which Cu^{I} oxidation is the sole kinetically-relevant step is nearly approached at 1 kPa O_2 on the lowest Cu density samples, while the zero-order kinetic regime in which Cu^{II} reduction is the sole kinetically-relevant step is nearly approached at 60 kPa O_2 on the highest density samples (Table 2). These data again remind that rates of Cu^{I} oxidation and Cu^{II} reduction steps depend both on the pressures of gaseous reactants involved and on Cu volumetric density in a manner that reflects the specific Cu site requirements of such steps. As a result, apparent rate constants that strictly correspond to first-order and zero-order kinetic regimes on a given Cu-CHA sample must be estimated by extrapolating measured rate data using a rate equation, as discussed next.

3.3. Dependence of apparent first-order rate constants on Cu volumetric density

Values of apparent first-order (k_{first}) and zero-order (k_{zero}) rate constants, determined by regressing the steady-state SCR rate data in Fig. 2b to Equation (3), are listed for each sample in Table 3. The dependence of k_{first} on Cu volumetric density in Cu-CHA (Si/Al = 15) is shown in Fig. 3. Values of k_{first} increase systematically with Cu volumetric density in the entire range of Cu density values studied (0.078–0.35 Cu per 1000 Å^3). A strictly linear dependence of k_{first} (per Cu) on Cu density is equivalent to a strictly second-order dependence of the SCR rate on Cu concentration, as would be expected for a mean-field rate expression for a homogeneous reaction involving two Cu sites. Yet, the oxidation of Cu^{I} sites in Cu-CHA by O_2 is not mean-field in nature; only a fraction of $Cu^{I}(NH_3)_2$ species are able to be oxidized by O_2 to form a binuclear Cu^{II} di-oxo complex, and the fraction of such oxidizable Cu^{I} sites increases with total Cu volumetric density [19]. Thus, we surmise that values of k_{first} deviate from a linear dependence on Cu density, especially apparent at low values of Cu density (Fig. 3), because of the non-mean-field kinetic behavior of O_2-assisted oxidation of $Cu^{I}(NH_3)_2$ species in Cu-CHA.

To investigate this behavior further, we performed transient XAS experiments during O_2-assisted oxidation of pre-reduced Cu-

Table 3
Measured first and zero order rate constants from steady-state SCR kinetics and intrinsic reduction and oxidation rate constants from transient kinetic experiments.

Sample	Steady-state measurements		Transient measurements		
	k_{zero} / 10^{-3} mol NO mol Cu^{-1} s^{-1}	k_{first} / 10^{-3} mol NO mol Cu^{-1} kPa O_2^{-1} s^{-1}	$k_{red}/10^{-3}$ s^{-1}	$k_{ox}/10^{-5}$ m^3 mol Cu^{-1} s^{-1}	Final Cu^{II} fraction after O_2 oxidation transient
Cu-CHA-0.078	10.7	0.18	20.4	14.1	0.67
Cu-CHA-0.084	9.1	0.27	18.4	–	–
Cu-CHA-0.10	7.5	0.24	–	7.9	0.77
Cu-CHA-0.17	16.1	0.80	10.2	8.1	0.78
Cu-CHA-0.23	15.6	1.09	7.4	7.1	0.85
Cu-CHA-0.29	14.8	1.87	–	7.8	0.83
Cu-CHA-0.31	16.4	1.76	–	14.5	0.85
Cu-CHA-0.35	18.2	2.80	21.1	12.4	0.81

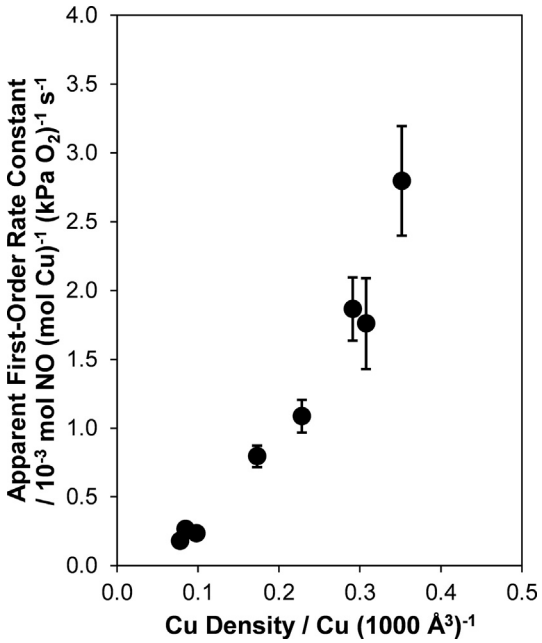

Fig. 3. Apparent first-order SCR rate constants (k_{first}, 473 K) as a function of Cu density.

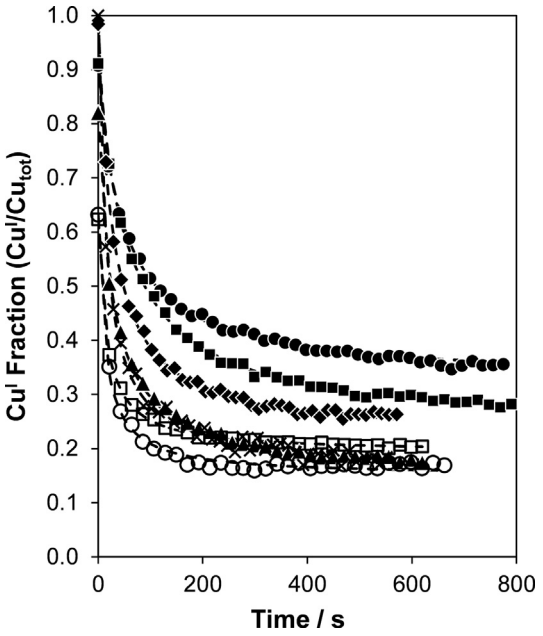

Fig. 4. Cu^I fraction (Cu^I/Cu_{tot}) from XAS experiments during transient O_2-assisted oxidation (10 kPa O_2, 473 K) of pre-reduced Cu-CHA-X samples (0.030 kPa NO, 0.030 kPa NH_3, 473 K): Cu-CHA-0.078 (●), Cu-CHA-0.10 (■), Cu-CHA-0.17 (♦), Cu-CHA-0.23 (▲), Cu-CHA-0.29 (×), Cu-CHA-0.31 (○), Cu-CHA-0.35 (□). Dotted lines represent least-squares regression of the data to a rate model second-order in Cu (details in Section S.7, SI).

CHA-X samples (seven samples of varying Cu density), analogous to such experiments reported in our prior study (on three Cu-CHA samples of varying Cu density) [19]. Cu-CHA samples were first reduced in flowing NO and NH_3 (0.030 kPa NO, 0.030 kPa NH_3, 473 K) to convert all Cu ions to $Cu^I(NH_3)_2$ species, followed by exposure to flowing O_2 (10 kPa O_2, 473 K) while monitoring time-resolved XAS spectra (XANES spectra in Figs. S13-S19, SI). Linear-combination fitting of XANES spectra were used to determine the fraction of Cu present in the $Cu^I(NH_3)_2$ state (Cu^I/Cu_{tot}) as a function of reaction time, as shown in Fig. 4.

For each Cu-CHA sample, regardless of Cu content, the transient Cu^I oxidation rate was best modeled using a rate law with a second-order dependence on Cu concentration that accounts for a recalcitrant fraction of un-oxidized Cu^I in the limit of long reaction time (details in Section S.7, SI) [19]. The fitted value for the intrinsic second-order rate constant for O_2-assisted oxidation (k_{ox}) of $Cu^I(NH_3)_2$ species is listed in Table 3. Values of k_{ox} are essentially invariant (within 2×, 473 K) for the range of Cu volumetric densities studied (0.078–0.35 Cu per 1000 Å^3). The fraction of Cu sites that were oxidized to the Cu^{II} state at the end of the transient O_2-oxidation experiment is also shown in Table 3; this fraction increased (0.67–0.85) with Cu volumetric density (0.078–0.35 Cu per 1000 Å^3), consistent with our prior work [19]. These findings are also consistent with data reported recently by Liu et al., in which O_2-assisted oxidation (473 K, 10 kPa O_2) of pre-reduced Cu-CHA (Si/Al = 15) resulted in higher fractions of oxidizable Cu(I) on a sample with higher Cu content (0.95, Cu/Al = 0.29) than on a sample of lower Cu content (0.53, Cu/Al = 0.03) [39].

We next sought to compare the rate measurements from transient Cu^I oxidation experiments performed at 10 kPa O_2 to the steady-state SCR rates measured in the first-order (i.e., "low" O_2 pressure) kinetic regime. The steady-state Cu^I oxidation rate expected at 10 kPa O_2 was estimated by multiplying k_{first} by this dioxygen pressure (10 kPa O_2), and these values are plotted on the primary ordinate of Fig. 5. Initial rates of Cu^I oxidation from the transient XAS experiments (at 10 kPa O_2) were estimated by extrapolating the fitted second-order rate models to initial time (details in Section S.7, SI), and these values are plotted on the secondary ordinate of Fig. 5. Both of these rates systematically increase with a similar functional dependence on Cu volumetric density (Fig. 5); the deviation from a strictly linear dependence on Cu volumetric density, as would have otherwise been expected for a mean-field rate expression for a dual-site Cu^I oxidation step, reflects the non-mean-field nature of this process.

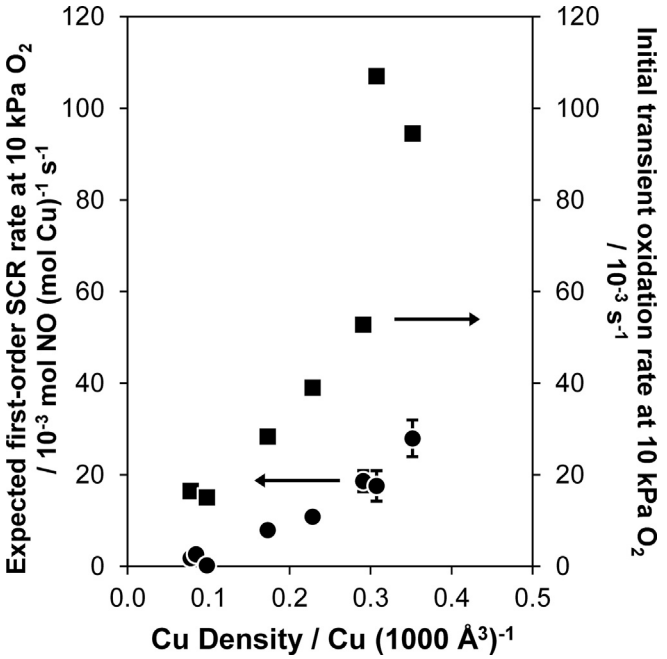

Fig. 5. Estimated Cu^{I}-oxidation-limited steady-state SCR rates (473 K) at 10 kPa O_2 (●) plotted along with initial Cu^{I} oxidation rates measured from transient XAS experiments (■), as a function of Cu density.

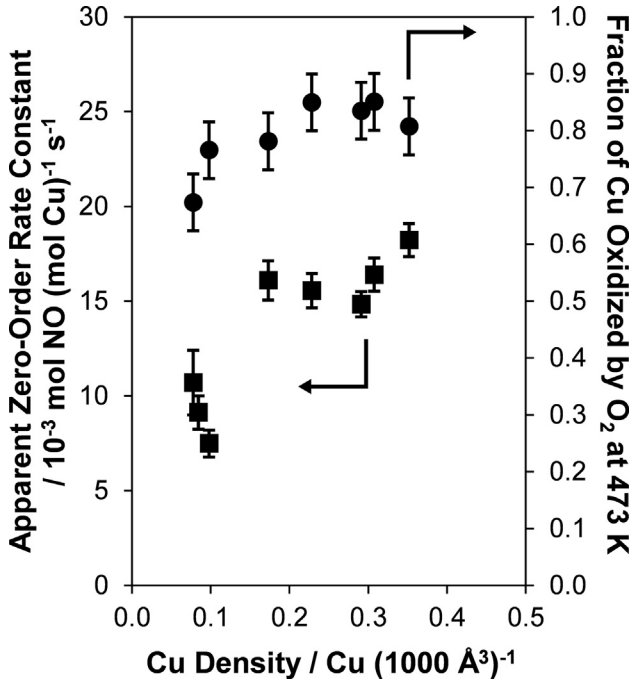

Fig. 6. Cu volumetric density dependence of apparent zero-order SCR rate constants (k_{zero}) at 473 K (■) and the fraction Cu^{I} that is oxidized to Cu^{II} after treatment in 10 kPa O_2 at 473 K (●) from the transient XAS experiments shown in Fig. 5.

3.4. Dependence of apparent zero-order rate constants on Cu spatial density

The dependence of k_{zero} on Cu volumetric density in Cu-CHA (Si/Al = 15) is shown in Fig. 6. In the entire range of Cu densities studied (0.078–0.35 Cu per 1000 Å^3), values of k_{zero} show a much weaker dependence on Cu density than k_{first} (Fig. 3). Values of k_{zero} are lower among the three samples of lowest Cu density (7.5–10.7 × 10^{-3} mol NO mol Cu^{-1} s^{-1}, Table 3) than among the five samples of higher Cu density (14.8–18.2 × 10^{-3} mol NO mol Cu^{-1} s^{-1}, Table 3). Values of k_{zero} also appear to become invariant of Cu density above the threshold value of 0.17 Cu per 1000 Å^3 in the sample composition studied. Such variations in k_{zero} with Cu density could, in principle, reflect changes in either the intrinsic rate constant for Cu^{II} reduction, or the fraction of Cu sites that participate in steady-state SCR turnovers.

To investigate the intrinsic reduction behavior of NH_3-solvated Cu^{II} sites in Cu-CHA, and its dependence on Cu volumetric density, we performed transient XAS experiments during NO + NH_3-assisted co-reduction of oxidized Cu-CHA-X samples (five samples of varying Cu density). Cu-CHA samples were first oxidized in flowing O_2 (20 kPa O_2, 673 K) to convert all Cu ions to zeolite-bound Cu^{II} species, followed by exposure to flowing NO and NH_3 (0.030 kPa NO, 0.030 kPa NH_3, 473 K) to solvate Cu^{II} ions with NH_3 to form $Cu^{II}(NH_3)_4$ or $Cu^{II}(OH)(NH_3)_3$ complexes and to subsequently reduce them to $Cu^{I}(NH_3)_2$, while monitoring time-resolved XAS spectra (XANES spectra in Figs. S20-S24, SI). Linear-combination fitting of XANES spectra were used to determine the fraction of Cu present in the NH_3-solvated Cu^{II} state (Cu^{II}/Cu_{tot}) as a function of reaction time, as shown in Fig. 7.

On all Cu-CHA samples, the transient Cu^{II} reduction rate showed a first-order dependence on Cu density (Fig. 7). In some samples, XANES spectra at the end of the transient NO + NH_3-assisted reduction experiments (Figs. S20-S24, SI) showed small percentages (≤10%) of Cu^{II} that were not reduced; these values are within the uncertainty of the linear combination XANES fitting procedure, but were explicitly accounted for when fitting the transient data

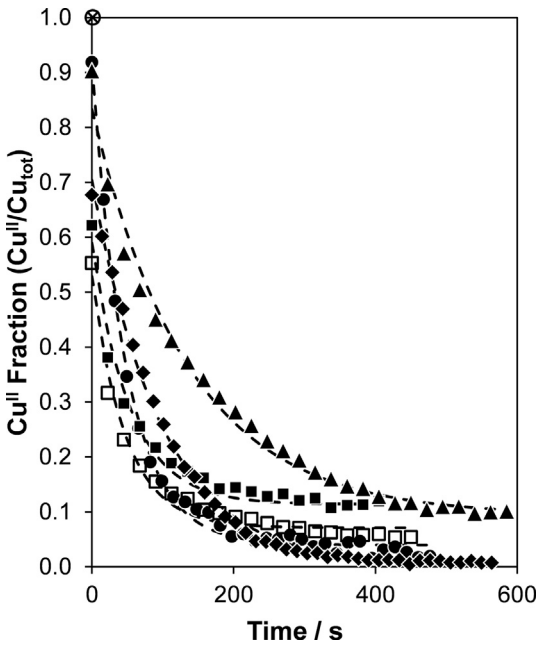

Fig. 7. Cu^{II} fraction (Cu^{II}/Cu_{tot}) from XAS experiments during transient NO + NH_3-assisted reduction (0.030 kPa NO, 0.030 kPa NH_3, 473 K) of oxidized Cu-CHA-X samples (20 kPa O_2, 673 K): Cu-CHA-0.078 (●), Cu-CHA-0.084 (■), Cu-CHA-0.17 (♦), Cu-CHA-0.23 (▲), and Cu-CHA-0.35 (□). Dotted lines are best fits to a rate equation that is first-order in Cu concentration (details in Section S.8, SI).

to a first-order rate equation (details in Section S.8, SI). Values of k_{red} were similar (within 3× at 473 K, 7.4–21.1 10^{-3} s^{-1}; Table 3) and did not vary systematically with Cu density. These values are quantitatively consistent with the initial rate of Cu^{II} reduction (1.7 mmol NO $g^{-1}h^{-1}$ at 0.05 kPa NO and 423 K) reported recently

on a Cu-CHA sample of similar composition (2 wt% Cu) [39], assuming a first-order dependence on NO pressure and an activation energy consistent with those reported for reduction-limited SCR kinetics (full calculation in Section S.8, SI) [6,19]. Similar Cu^{II} reduction rate constants measured among Cu-CHA samples of different Cu density would also be consistent with the proposed single-site mechanism of NO and NH_3-assisted co-reduction of mononuclear NH_3-solvated Cu^{II} sites [9,16].

Thus, we considered the alternate possibility that k_{zero} values are influenced by the fraction of Cu sites that participate in steady-state SCR turnover. This fraction of active Cu was estimated to be the fraction of $Cu^{I}(NH_3)_2$ that was oxidized by O_2 at the end of transient XAS experiments shown in Fig. 4; as listed in Table 3, they increase (0.67–0.85) with Cu density (0.078–0.35 Cu per 1000 A^3). These values are plotted on the secondary ordinate of Fig. 6, and show a similar functional dependence on Cu density as k_{zero}. This indicates that the dependence of k_{zero} (normalized per Cu_{tot}) on Cu volumetric density primarily reflects changes in the fraction of Cu sites that participate in steady-state SCR redox cycles, specifically in the dual-site O_2-assisted oxidation half-cycle.

4. Conclusions

The selective catalytic reduction (SCR) of NO with NH_3 on Cu-CHA zeolites is mediated by NH_3-solvated Cu^{II} and Cu^{I} ions at low temperatures (<523 K), and occurs via a Cu^{II}/Cu^{I} redox cycle involving single-site Cu^{II} reduction assisted by NO and NH_3 and dual-site Cu^{I} oxidation assisted by O_2. When low-temperature SCR rates are measured at fixed reaction conditions (e.g., "standard" SCR conditions), they depend on the rates of both Cu^{II} reduction and Cu^{I} oxidation processes. With increasing Cu density, SCR rates (per Cu) transition from a second-order to first-order dependence on Cu density, Cu^{II} fractions measured *in operando* by XAS systematically increase, and apparent reaction orders in O_2 systematically decrease. The kinetic influences of Cu^{I} oxidation and Cu^{II} reduction processes are convoluted in apparent kinetic parameters measured under "standard" SCR conditions, obfuscating the individual influences of Cu-zeolite structure and composition on the fraction of Cu sites that participate in SCR turnovers and on the rate constants for Cu^{I} oxidation and Cu^{II} reduction processes.

Low-temperature (473 K) SCR rates on Cu-CHA show a Langmuirian dependence on dioxygen pressure when varied widely (1–60 kPa O_2), and approach a first-order dependence in the "low O_2 pressure" limit and a zero-order dependence in the "high O_2 pressure" limit. Yet, even when SCR rates are measured at fixed pressure in the "low O_2 pressure" limit (e.g., 1 kPa O_2), *in operando* characterization reveals that a fraction of Cu in Cu-CHA is present in the Cu^{II} state, and this fraction increases systematically with increasing Cu density. This serves as yet another reminder that differences in kinetic behavior among catalysts of varying composition are more accurately evaluated through comparisons of rate constants, not turnover rates measured at fixed reaction conditions. This is especially pertinent for catalytic cycles comprised of elementary steps that have different active site density requirements, for which changes in catalyst composition will change the kinetic relevance of each step.

Steady-state SCR rates measured over widely varying dioxygen pressures enable estimating apparent first-order (k_{first}) and zero-order (k_{zero}) rate constants that reflect SCR redox cycles limited by dual-site Cu^{I} oxidation with O_2 and by single-site Cu^{II} reduction with NO and NH_3, respectively. On Cu-CHA zeolites, values of k_{first} (per Cu, 473 K) increase with Cu density, according to a functional dependence consistent with the dual-site and non-mean-field nature of O_2-assisted Cu^{I} oxidation steps. Values of k_{zero} (per Cu, 473 K) show a weaker dependence on Cu density, a consequence of its underlying dependence on the fraction of Cu sites that can participate in SCR redox cycles and specifically in O_2-assisted Cu^{I} oxidation steps. Importantly, among Cu-CHA samples of varying composition that are comprised nominally of isolated Cu ions, the mechanisms of Cu^{I} oxidation and Cu^{II} reduction do not appear to change; rather the relative intrinsic rates of these processes change with reaction conditions due to their differing kinetic and site requirements, and neither one solely limits the rates of the SCR redox cycle.

As illustrated here for low-temperature NO_x SCR with NH_3 on Cu-CHA zeolites, such phenomena can be identified by measuring reaction rates under varying reaction conditions to isolate kinetic regimes wherein rates of certain elementary steps limit rates of the overall catalytic cycle. Such rate measurements facilitate precise mechanistic interpretation, when complemented with measurements of transient rates of stoichiometric reactions that are proposed facsimiles of the elementary steps that prevail during steady-state catalytic turnover, and *in operando* spectroscopy to determine the structures of the relevant MARI [40]. The measurement of steady-state SCR rates over widely varying dioxygen pressures, in order to estimate apparent first-order and zero-order rate constants in O_2 pressure, enables quantitative comparisons of reactivity among Cu-zeolite catalysts of different Cu content. We expect these conclusions will apply for low-temperature NO_x SCR catalysis on other Cu-based materials, under conditions wherein the reactive intermediates are NH_3-solvated Cu ions and O_2 is the oxidant used in Cu^{I} oxidation half-cycles. The approach used here can also quantitatively describe how other catalyst properties, such as zeolite framework topology and framework Al density and arrangement, influence the fraction of Cu sites that participate in SCR redox cycles and the rates at which they catalyze relevant Cu^{I} oxidation and Cu^{II} reduction processes.

Declaration of Competing Interest

None.

Acknowledgements

We acknowledge financial support provided by the National Science Foundation CAREER program under award number 1552517-CBET. Use of the Advanced Photon Source is supported by the U.S. Department of Energy, Office of Science, and Office of Basic Energy Sciences, under Contract no. DE-AC02-06CH11357. MRCAT operations and beamline 10-BM are supported by the Department of Energy and the MRCAT member institutions. We thank Prof. Christopher Paolucci (Virginia), Trevor M. Lardinois (Purdue), Dr. John Di Iorio (Purdue) and Dr. Atish Parekh (Purdue) for helpful technical discussions. We also thank Sachem, Inc. for providing the organic structure-directing agent used to synthesize SSZ-13.

Appendix A. Supplementary material

Supplementary data to this article can be found online at https://doi.org/10.1016/j.jcat.2020.05.022.

References

[1] C.H.F. Peden, Cu/Chabazite Catalysts for 'Lean-Burn' Vehicle Emission Control, J. Catal. 373 (2019) 384–389, https://doi.org/10.1016/j.jcat.2019.04.046.
[2] I. Bull, R.S. Boorse, W.M. Jaglowski, G.S. Koermer, A. Moini, J.A. Patchett, W.-M. Xue, P. Burk, J.C. Dettling, M.T. Caudle, Copper CHA Zeolinte Catalysts, US20080226545A1, 2008.
[3] P.J. Andersen, J.E. Bailie, J.L. Casci, H.-Y. Chen, J.M. Fedeyko, R.K.S. Foo, R.R. Rajaram, Transition Metal/Zeolite SCR Catalysts, WO2008132452A2, (2008).
[4] C. Paolucci, J.R. Di Iorio, F.H. Ribeiro, R. Gounder, W.F. Schneider, Chapter One - Catalysis Science of NOx Selective Catalytic Reduction With Ammonia Over Cu-

SSZ-13 and Cu-SAPO-34, in: C. Song (Ed.), Adv. Catal., Academic Press, 2016: pp. 1–107. https://doi.org/10.1016/bs.acat.2016.10.002.
[5] K. Kamasamudram, N. Currier, T. Szailer, A. Yezerets, Why Cu- and Fe-Zeolite SCR Catalysts Behave Differently At Low Temperatures, SAE Int. J. Fuels Lubr. 3 (2010) 664–672, https://doi.org/10.4271/2010-01-1182.
[6] F. Gao, D. Mei, Y. Wang, J. Szanyi, C.H.F. Peden, Selective Catalytic Reduction over Cu/SSZ-13: Linking Homo- and Heterogeneous Catalysis, J. Am. Chem. Soc. 139 (2017) 4935–4942, https://doi.org/10.1021/jacs.7b01128.
[7] K.A. Lomachenko, E. Borfecchia, C. Negri, G. Berlier, C. Lamberti, P. Beato, H. Falsig, S. Bordiga, The Cu-CHA deNO$_x$ Catalyst in Action: Temperature-Dependent NH$_3$-Assisted Selective Catalytic Reduction Monitored by Operando XAS and XES, J. Am. Chem. Soc. 138 (2016) 12025–12028, https://doi.org/10.1021/jacs.6b06809.
[8] A.R. Fahami, T. Günter, D.E. Doronkin, M. Casapu, D. Zengel, T.H. Vuong, M. Simon, F. Breher, A.V. Kucherov, A. Brückner, J.-D. Grunwaldt, The Dynamic Nature of Cu Sites in Cu-SSZ-13 and the Origin of the Seagull NO$_x$ Conversion Profile During NH$_3$-SCR, React. Chem. Eng. 4 (2019) 1000–1018, https://doi.org/10.1039/C8RE00290H.
[9] C. Paolucci, A.A. Parekh, I. Khurana, J.R. Di Iorio, H. Li, J.D. Albarracin Caballero, A.J. Shih, T. Anggara, W.N. Delgass, J.T. Miller, F.H. Ribeiro, R. Gounder, W.F. Schneider, Catalysis in a Cage: Condition-Dependent Speciation and Dynamics of Exchanged Cu Cations in SSZ-13 Zeolites, J. Am. Chem. Soc. 138 (2016) 6028–6048, https://doi.org/10.1021/jacs.6b02651.
[10] E. Borfecchia, K.A. Lomachenko, F. Giordanino, H. Falsig, P. Beato, A.V. Soldatov, S. Bordiga, C. Lamberti, Revisiting the Nature of Cu Sites in the Activated Cu-SSZ-13 Catalyst for SCR Reaction, Chem. Sci. 6 (2014) 548–563, https://doi.org/10.1039/C4SC02907K.
[11] F. Giordanino, P.N.R. Vennestrøm, L.F. Lundegaard, F.N. Stappen, S. Mossin, P. Beato, S. Bordiga, C. Lamberti, Characterization of Cu-exchanged SSZ-13: A Comparative FTIR, UV-Vis, and EPR study with Cu-ZSM-5 and Cu-β with Similar Si/Al and Cu/Al Ratios, Dalton Trans. 42 (2013) 12741–12761, https://doi.org/10.1039/C3DT50732G.
[12] V.F. Kispersky, A.J. Kropf, F.H. Ribeiro, J.T. Miller, Low Absorption Vitreous Carbon Reactors for *Operando* XAS: A Case Study on Cu/Zeolites for Selective Catalytic Reduction of NO$_x$ by NH$_3$, Phys. Chem. Chem. Phys. 14 (2012) 2229–2238, https://doi.org/10.1039/C1CP22992C.
[13] T. Günter, D.E. Doronkin, A. Boubnov, H.W.P. Carvalho, M. Casapu, J.-D. Grunwaldt, The SCR of NO$_x$ with NH$_3$ Examined by Novel X-ray Emission and X-ray Absorption Methods, Top. Catal. 59 (2016) 866–874, https://doi.org/10.1007/s11244-016-0561-7.
[14] T.V.W. Janssens, H. Falsig, L.F. Lundegaard, P.N.R. Vennestrøm, S.B. Rasmussen, P.G. Moses, F. Giordanino, E. Borfecchia, K.A. Lomachenko, C. Lamberti, S. Bordiga, A. Godiksen, S. Mossin, P. Beato, A Consistent Reaction Scheme for the Selective Catalytic Reduction of Nitrogen Oxides with Ammonia, ACS Catal. 5 (2015) 2832–2845, https://doi.org/10.1021/cs501673g.
[15] J. Luo, F. Gao, K. Kamasamudram, N. Currier, C.H.F. Peden, A. Yezerets, New Insights into Cu/SSZ-13 SCR Catalyst Acidity. Part I: Nature of Acidic Sites Probed by NH$_3$ Titration, J. Catal. 348 (2017) 291–299, https://doi.org/10.1016/j.jcat.2017.02.025.
[16] C. Paolucci, A.A. Verma, S.A. Bates, V.F. Kispersky, J.T. Miller, R. Gounder, W.N. Delgass, F.H. Ribeiro, W.F. Schneider, Isolation of the Copper Redox Steps in the Standard Selective Catalytic Reduction on Cu-SSZ-13, Angew. Chem. Int. Ed. 53 (2014) 11828–11833, https://doi.org/10.1002/anie.201407030.
[17] F. Giordanino, E. Borfecchia, K.A. Lomachenko, A. Lazzarini, G. Agostini, E. Gallo, A.V. Soldatov, P. Beato, S. Bordiga, C. Lamberti, Interaction of NH$_3$ with Cu-SSZ-13 Catalyst: A Complementary FTIR, XANES, and XES Study, J. Phys. Chem. Lett. 5 (2014) 1552–1559, https://doi.org/10.1021/jz500241m.
[18] R. Villamaina, S. Liu, I. Nova, E. Tronconi, M.P. Ruggeri, J. Collier, A. York, D. Thompsett, Speciation of Cu Cations in Cu-CHA Catalysts for NH$_3$-SCR: Effects of SiO$_2$/AlO$_3$ Ratio and Cu-Loading Investigated by Transient Response Methods, ACS Catal. 9 (2019) 8916–8927, https://doi.org/10.1021/acscatal.9b02578.
[19] C. Paolucci, I. Khurana, A.A. Parekh, S. Li, A.J. Shih, H. Li, J.R. Di Iorio, J.D. Albarracin-Caballero, A. Yezerets, J.T. Miller, W.N. Delgass, F.H. Ribeiro, W.F. Schneider, R. Gounder, Dynamic Multinuclear Sites Formed by Mobilized Copper Ions in NO$_x$ Selective Catalytic Reduction, Science. 357 (2017) 898–903, https://doi.org/10.1126/science.aan5630.
[20] T. Selleri, M.P. Ruggeri, I. Nova, E. Tronconi, The Low Temperature Interaction of NO + O$_2$ with a Commercial Cu-CHA Catalyst: A Chemical Trapping Study, Top. Catal. 59 (2016) 678–685, https://doi.org/10.1007/s11244-016-0543-9.
[21] L.M. Mirica, X. Ottenwaelder, T.D.P. Stack, Structure and Spectroscopy of Copper–Dioxygen Complexes, Chem. Rev. 104 (2004) 1013–1046, https://doi.org/10.1021/cr020632z.
[22] C.E. Elwell, N.L. Gagnon, B.D. Neisen, D. Dhar, A.D. Spaeth, G.M. Yee, W.B. Tolman, Copper-Oxygen Complexes Revisited: Structures, Spectroscopy, and Reactivity, Chem. Rev. 117 (2017) 2059–2107, https://doi.org/10.1021/acs.chemrev.6b00636.
[23] E.A. Lewis, W.B. Tolman, Reactivity of Dioxygen–Copper Systems, Chem. Rev. 104 (2004) 1047–1076, https://doi.org/10.1021/cr020633r.
[24] L. Chen, H. Falsig, T.V.W. Janssens, H. Grönbeck, Activation of Oxygen on $(NH_3CuNH_3)^+$ in NH$_3$-SCR over Cu-CHA, J. Catal. 358 (2018) 179–186, https://doi.org/10.1016/j.jcat.2017.12.009.
[25] L. Chen, T.V.W. Janssens, H. Grönbeck, A Comparative Test of Different Density Functionals for Calculations of NH$_3$-SCR over Cu-Chabazite, Phys. Chem. Chem. Phys. 21 (2019) 10923–10930, https://doi.org/10.1039/C9CP01576K.
[26] F. Gao, E.D. Walter, M. Kollar, Y. Wang, J. Szanyi, C.H.F. Peden, Understanding Ammonia Selective Catalytic Reduction Kinetics over Cu/SSZ-13 from Motion of the Cu Ions, J. Catal. 319 (2014) 1–14, https://doi.org/10.1016/j.jcat.2014.08.010.
[27] F. Gao, N.M. Washton, Y. Wang, M. Kollár, J. Szanyi, C.H.F. Peden, Effects of Si/Al Ratio on Cu/SSZ-13 NH$_3$-SCR Catalysts: Implications for the Active Cu Species and the Roles of Brønsted Acidity, J. Catal. 331 (2015) 25–38, https://doi.org/10.1016/j.jcat.2015.08.004.
[28] L. Chen, H. Falsig, T.V.W. Janssens, J. Jansson, M. Skoglundh, H. Grönbeck, Effect of Al-Distribution on Oxygen Activation over Cu–CHA, Catal. Sci. Technol. 8 (2018) 2131–2136, https://doi.org/10.1039/C8CY00083B.
[29] A. Marberger, A.W. Petrov, P. Steiger, M. Elsener, O. Kröcher, M. Nachtegaal, D. Ferri, Time-resolved Copper Speciation During Selective Catalytic Reduction of NO on Cu-SSZ-13, Nat. Catal. 1 (2018) 221–227, https://doi.org/10.1038/s41929-018-0032-6.
[30] S.A. Bates, W.N. Delgass, F.H. Ribeiro, J.T. Miller, R. Gounder, Methods for NH$_3$ Titration of Brønsted Acid Sites in Cu-zeolites that Catalyze the Selective Catalytic Reduction of NO$_x$ with NH$_3$, J. Catal. 312 (2014) 26–36, https://doi.org/10.1016/j.jcat.2013.12.020.
[31] J.R. Di Iorio, S.A. Bates, A.A. Verma, W.N. Delgass, F.H. Ribeiro, J.T. Miller, R. Gounder, The Dynamic Nature of Brønsted Acid Sites in Cu–Zeolites During NO$_x$ Selective Catalytic Reduction: Quantification by Gas-Phase Ammonia Titration, Top. Catal. 58 (2015) 424–434, https://doi.org/10.1007/s11244-015-0387-8.
[32] A.J. Kropf, J. Katsoudas, S. Chattopadhyay, T. Shibata, E.A. Lang, V.N. Zyryanov, B. Ravel, K. McIvor, K.M. Kemner, K.G. Scheckel, S.R. Bare, J. Terry, S.D. Kelly, B. A. Bunker, C.U. Segre, The New MRCAT (Sector 10) Bending Magnet Beamline at the Advanced Photon Source, AIP Conf. Proc. 1234 (2010) 299–302, https://doi.org/10.1063/1.3463194.
[33] S.A. Bates, A.A. Verma, C. Paolucci, A.A. Parekh, T. Anggara, A. Yezerets, W.F. Schneider, J.T. Miller, W.N. Delgass, F.H. Ribeiro, Identification of the Active Cu Site in Standard Selective Catalytic Reduction with Ammonia on Cu-SSZ-13, J. Catal. 312 (2014) 87–97, https://doi.org/10.1016/j.jcat.2014.01.004.
[34] R.M. Koros, E.J. Nowak, A Diagnostic Test of the Kinetic Regime in a Packed Bed Reactor, Chem. Eng. Sci. 22 (1967) 470, https://doi.org/10.1016/0009-2509(67)80134-9.
[35] P.B. Weisz, C.D. Prater, Interpretation of Measurements in Experimental Catalysis, in: W.G. Frankenburg, V.I. Komarewsky, E.K. Rideal (Eds.), Adv. Catal., Academic Press, 1954: pp. 143–196. https://doi.org/10.1016/S0360-0564(08)60390-9.
[36] A.J. Shih, I. Khurana, H. Li, J. González, A. Kumar, C. Paolucci, T.M. Lardinois, C.B. Jones, J.D. Albarracin Caballero, K. Kamasamudram, A. Yezerets, W.N. Delgass, J.T. Miller, A.L. Villa, W.F. Schneider, R. Gounder, F.H. Ribeiro, Spectroscopic and Kinetic Responses of Cu-SSZ-13 to SO$_2$ Exposure and Implications for NO$_x$ Selective Catalytic Reduction, Appl. Catal. A 574 (2019) 122–131, https://doi.org/10.1016/j.apcata.2019.01.024.
[37] Y. Jangjou, C.S. Sampara, Y. Gu, D. Wang, A. Kumar, J. Li, W.S. Epling, Mechanism-based Kinetic Modeling of Cu-SSZ-13 Sulfation and Desulfation for NH$_3$-SCR Applications, React. Chem. Eng. 4 (2019) 1038–1049, https://doi.org/10.1039/C8RE00210J.
[38] G. Cavataio, J. Girard, J.E. Patterson, C. Montreuil, Y. Cheng, C.K. Lambert, Laboratory Testing of Urea-SCR Formulations to Meet Tier 2 Bin 5 Emissions, in: 2007: pp. 2007-01–1575. https://doi.org/10.4271/2007-01-1575
[39] C. Liu, H. Kubota, T. Amada, K. Kon, T. Toyao, Z. Maeno, K. Ueda, J. Ohyama, A. Satsuma, T. Tanigawa, N. Tsunoji, T. Sano, K. Shimizu, In Situ Spectroscopic Studies on the Redox Cycle of NH$_3$–SCR over Cu-CHA Zeolites, ChemCatChem 12 (2020) 3050–3059, https://doi.org/10.1002/cctc.202000024.
[40] S.H. Krishna, C.B. Jones, J.T. Miller, F.H. Ribeiro, R. Gounder, Combining Kinetics and *Operando* Spectroscopy to Interrogate the Mechanism and Active Site Requirements of NO$_x$ Selective Catalytic Reduction with NH$_3$ on Cu-Zeolites, J. Phys. Chem. Lett. (2020), https://doi.org/10.1021/acs.jpclett.0c00903.

SUPPORTING INFORMATION

Effects of Dioxygen Pressure on Rates of NO_x Selective Catalytic Reduction with NH_3 on Cu-CHA Zeolites

Casey B. Jones[1,†], Ishant Khurana[1,†], Siddarth H. Krishna[1], Arthur J. Shih[1], W. Nicholas Delgass[1], Jeffrey T. Miller[1], Fabio H. Ribeiro[1], William F. Schneider[2], Rajamani Gounder[1,*]

[1]*Charles D. Davidson School of Chemical Engineering, Purdue University, 480 Stadium Mall Drive, West Lafayette, IN 47907, USA*

[2]*Department of Chemical and Biomolecular Engineering, University of Notre Dame, 250 Nieuwland Science Hall, Notre Dame, IN 46556, USA*

[†]C. B. J. and I. K. contributed equally to this work.

*Corresponding author: rgounder@purdue.edu

Section S.1. Characterization data of H-CHA zeolite samples

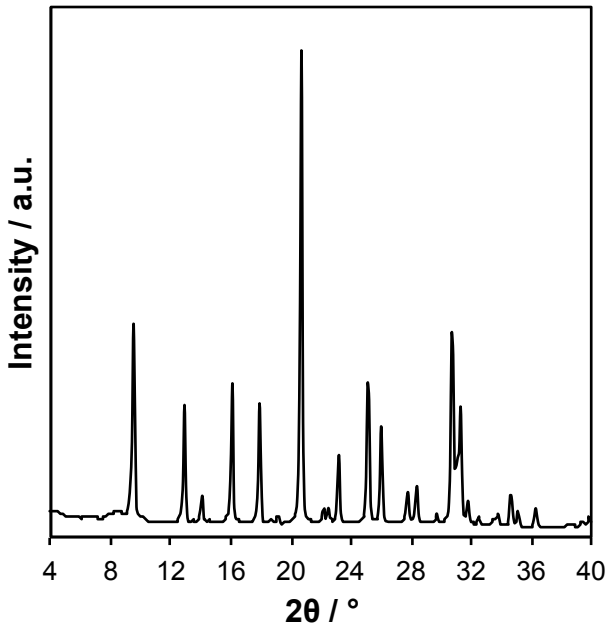

Figure S1. X-Ray diffraction pattern of a representative parent H-CHA (Si/Al = 15) sample prepared using methods reported in Paolucci et al. [1]

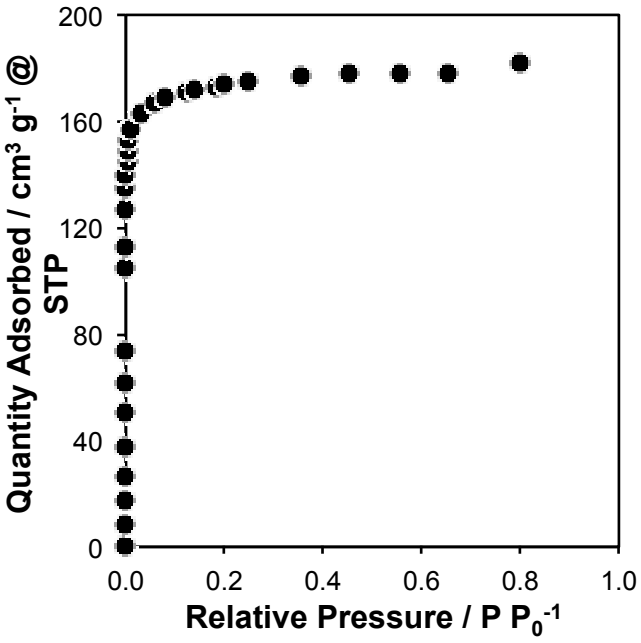

Figure S2. Ar adsorption isotherm (87 K) on a representative parent H-CHA (Si/Al = 15) sample prepared using methods reported in Paolucci et al. [1]

Section S.2. Characterization of Cu-CHA zeolites with varying Cu ion density

Cu-CHA samples with varying spatial density of isolated Cu sites (present either as Cu^{II} at paired framework Al or as $[Cu^{II}OH]^+$ at isolated framework Al) were studied here, as in our previous study [1]. These samples are denoted Cu-CHA-X, where X refers to the volumetric Cu density (atoms Cu per 1000 $Å^3$). Relevant structural and site characterization of these samples are provided in Table S1, including bulk elemental analysis, the number of Cu^{II} and $[Cu^{II}OH]^+$ sites (per Al), the concentration of Cu ions per crystallite volume, and the mean Cu-Cu distance. Additional Cu site characterization (*ex situ* X-ray absorption and UV-Visible spectra) can be found in our previous study [2].

Table S1. Characterization data of oxidized Cu^{II} forms of Cu-CHA-X samples (X = Cu volumetric density per 1000 $Å^3$). Elemental analysis, number of H^+ sites titrated by NH_3 on H-CHA and Cu-CHA samples, number of isolated Cu^{II} and $[Cu^{II}OH]^+$ sites, concentration of Cu ions per crystallite volume, and the mean Cu-Cu distance. Characterization data originally reported in our prior study [2].

Sample	Number of H^+ sites		Number of Cu sites			Cu / 1000 $Å^3$	Mean Cu-Cu distance (Å)
	H^+/Al (H-form)[a]	H^+/Al (Cu-form)	Cu/Al	Cu^{II}/Al*	$Cu^{II}OH$/Al*		
Cu-CHA-0.078	0.98	0.81	0.08	0.08	0.00	0.078	29.0
Cu-CHA-0.084	0.98	-	0.09	-	-	0.084	28.3
Cu-CHA-0.10	0.98	0.80	0.10	0.08	0.02	0.10	26.9
Cu-CHA-0.17	0.98	0.70	0.18	0.10	0.08	0.17	22.3
Cu-CHA-0.23	1.00	0.64	0.24	0.12	0.12	0.23	20.3
Cu-CHA-0.29	1.00	0.61	0.31	0.08	0.23	0.29	18.7
Cu-CHA-0.31	0.98	0.58	0.33	0.09	0.22	0.31	18.4
Cu-CHA-0.35	0.98	0.51	0.37	0.10	0.27	0.35	17.6

[a] Different parent samples of H-CHA (Si/Al = 15), from replicate syntheses, were used to prepare the Cu-form samples.

*Determined from a site balance considering total Cu/Al, the number of H^+ titrated on H-form and Cu-form samples, and the 2:1 and 1:1 H^+:Cu exchange stoichiometry expected for Cu^{II} and $Cu^{II}OH$, respectively.

Section S.3. Methods used to measure and calculate NO SCR rates by correcting for contributions of "fast" SCR reactions from NO_2

All reported NO SCR rates were corrected for contributions from the "fast" SCR reaction due to background NO_2, which is present as an impurity in NO cylinders and is formed by gas-phase NO oxidation. A blank reactor tube was loaded with 0.070 g SiO_2 to measure background NO_2 formation rates at fixed NO pressure (0.03 kPa) at 473 K, but with varying O_2 pressures (0.5–60 kPa O_2) and total gas flow rates (1.0–2.5 L min^{-1} at ambient temperature and pressure) (Fig. S3a). The gas-phase NO_2 concentration in the reactor outlet was linearly proportional to O_2 pressure (P_{O2}) and inversely proportional to gas flow rate F (i.e., proportional to gas residence time), with a constant of proportionality k, as shown in Figure S3a and as described by Equation (S1); the non-zero y-intercept b reflects NO_2 present as impurity levels in the NO cylinder.

$$[NO_2, background] = b + k(\frac{P_{O2}}{F})\,(\frac{P_{NO}}{0.03\ kPa\ NO})^2 \quad \text{(S1)}$$

NO_2 formation rates that show a first-order dependence on O_2 pressure and second-order dependence on NO pressure are consistent with gas-phase NO oxidation kinetics [3]. Background NO_2 formation rates indeed showed a nearly second-order dependence in NO pressure (0.015–0.060 kPa) (Fig. S3b). In order to correct for background NO_2 formation for experiments in which the NO pressure was varied from 0.03 kPa, such as when NO reaction orders were measured, Equation S1 also accounts for the second-order dependence of NO_2 formation rates on NO pressure. For these experiments, the y-intercept (b) of Figure S3a was also adjusted based on measurements of NO_2 concentration at 0 kPa O_2 and different NO pressures. Given that the background NO_2 concentration depends on the reactant source (e.g., NO_2 impurities in the NO cylinder) and reactor size and hydrodynamics (e.g., internal volumes of the reactor and gas lines, gas mixing patterns, gas residence time), the NO_2 background

concentration must be independently measured for each reactor system and NO cylinder used to measure SCR rates.

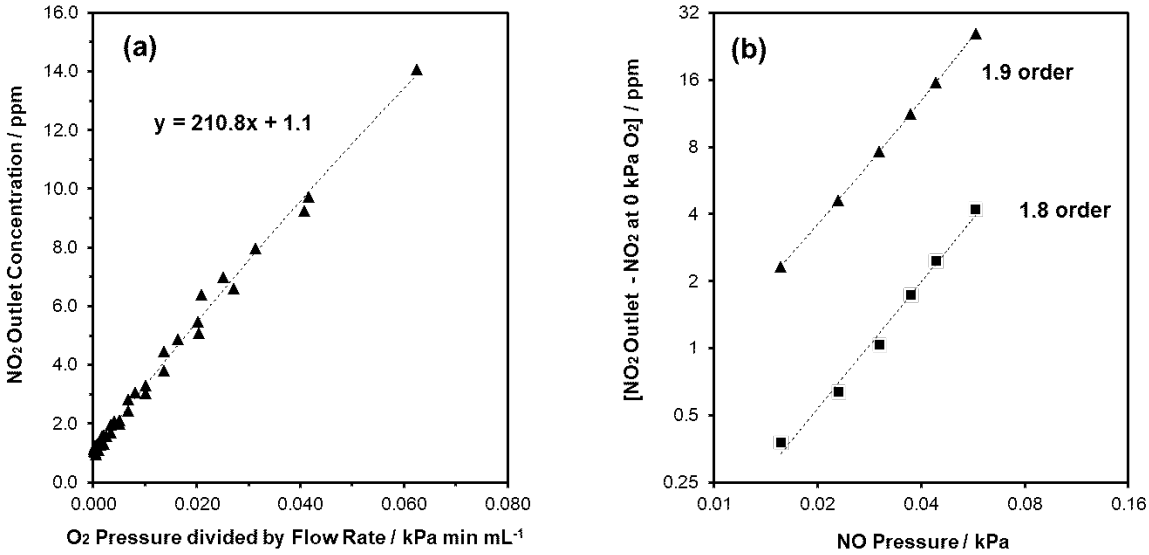

Figure S3. NO_2 concentration in reactor outlet of blank reactor experiments (SiO_2 only). (a) Variation of residence times and O_2 pressures. Dotted line represents regression of the data to Eq. (S1) (reaction conditions: 0.030 kPa NO, 0.030 kPa NH_3, 1–60 kPa O_2, 7 kPa CO_2, 1 kPa H_2O and balance N_2, 1.0–2.5 L min^{-1} total gas flow rate). (b) Variation of NO pressure. Linear fits were used to calculate NO reaction orders (reaction conditions: 0.015–0.060 kPa NO, 0.030 kPa NH_3, 10 (■) or 60 kPa (▲) O_2, 7 kPa CO_2, 1 kPa H_2O and balance N_2, 2.0 L min^{-1} total gas flow rate).

In experiments with Cu-CHA catalysts, the NO_2 consumed over the catalyst bed was calculated as the difference between NO_2 formed in the blank reactor and NO_2 measured in the outlet of the reactor in each experiment (Equation S2).

$$NO_2\ consumed\ = NO_2, background - NO_2, reactor\ outlet \quad \text{(S2)}$$

NO_2 consumption is assumed to occur through a "fast" SCR pathway, which consumes an equimolar amount of NO:

$$4\,NH_3 + 2\,NO + 2\,NO_2 \rightarrow 4\,N_2 + 6\,H_2O \quad \text{(S3)}$$

To calculate the rate of "standard" NO SCR, NO_2 consumption was subtracted from the total NO consumption:

$$NO_2\ consumed, standard\ SCR\ = NO\ consumed - NO_2\ consumed \quad \text{(S4)}$$

The ratio of "NO_2 consumed" to "NO consumed" is shown as a function of O_2 pressure for a representative sample (Cu-CHA-0.23) in Figure S4. For this sample, the magnitude of the "fast SCR correction" is 5-10% of the total NO consumption across all measured O_2 pressures.

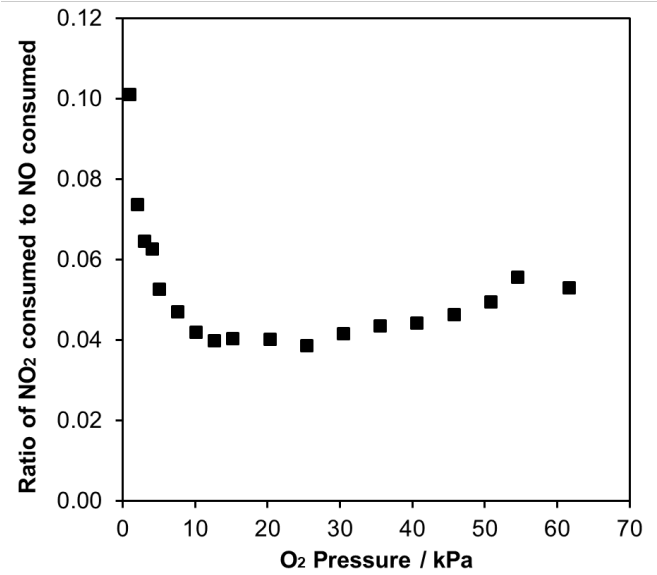

Figure S4. Ratio of "NO_2 consumed" to "NO consumed" as a function of O_2 pressure for Cu-CHA-0.23 (reaction conditions: 0.030 kPa NO, 0.030 kPa NH_3, 1–60 kPa O_2, 7 kPa CO_2, 1kPa H_2O and balance N_2).

For each Cu-CHA zeolite sample, SCR rates (473 K) at twenty O_2 pressures between 1–60 kPa were measured in random order, holding the concentration of other gases fixed (1 kPa H_2O, 7 kPa CO_2, 0.030 kPa NO, 0.030 kPa NH_3, balance N_2) while maintaining differential conversion. Figure S5 shows SCR rates as a function of varying O_2 pressure measured on Cu-CHA-0.23 in two different flow reactor systems of different internal volumes; the agreement between these measurements validates the methods described here to measure and calculate NO SCR rates.

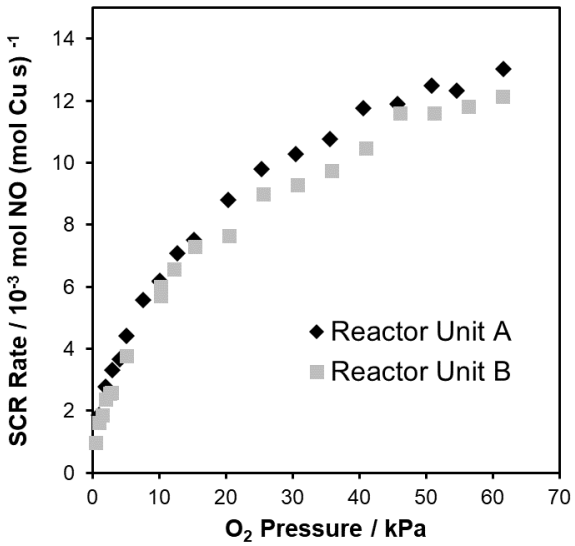

Figure S5. NO SCR rates (per Cu, 473 K) as a function of O_2 pressure in two separate reactor units for Cu-CHA-0.23 (reaction conditions: 0.030 kPa NO, 0.030 kPa NH_3, 1–60 kPa O_2, 7 kPa CO_2, 1 kPa H_2O and balance N_2). In order to account for background NO_2 formation in each reactor unit, the values of k and b in Equation S1 were measured independently for each system: Reactor Unit A (black diamonds), k = 210.9 (ppm mL min^{-1} kPa^{-1}); b = 0.73 ppm. Reactor Unit B (grey squares), k = 129.6 (ppm mL min^{-1} kPa^{-1}); b = 1.6 ppm.

Section S.4. Assessment of potential corruption of measured rates by transport phenomena

In order to assess the extent to which external transport phenomena influenced measured SCR rates, the gas hourly space velocity was varied from 1.13–2.26 (10^6 hr^{-1}) by varying total gas flow rates (1–2 L min^{-1} at ambient temperature and pressure) for Cu-CHA-0.084 at different O_2 pressures (1, 10, 30, and 60 kPa O_2). SCR rates were invariant with space velocity at all O_2 pressures (Figure S6), indicating that measured rates were uncorrupted by external transport processes, and confirming the absence of bed-scale gradients in concentration or temperature. The invariance of measured NO SCR rates with gas flow rate also shows that measured reaction rates are not influenced by changes to the gas-phase NO_2 concentration at the front of the catalyst bed.

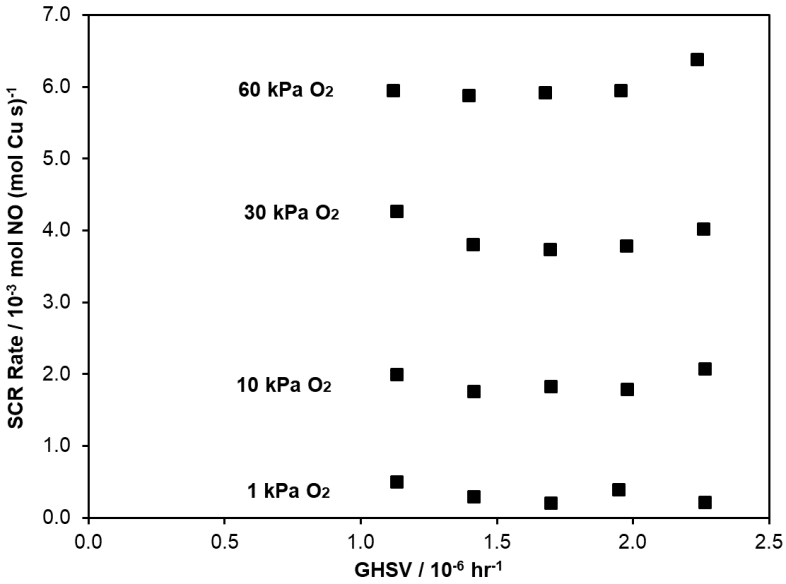

Figure S6. NO SCR rates (per Cu, 473 K) for Cu-CHA-0.084 as a function of gas hourly space velocity (reaction conditions: 0.030 kPa NO, 0.030 kPa NH_3, 1/10/30/60 kPa O_2, 7 kPa CO_2, 1 kPa H_2O and balance N_2).

The Weisz-Prater criterion (Equation S5) was used to estimate whether intracrystalline mass transport limitations affected measured rate data, and was calculated separately for O_2, NO, and NH_3, according to the following equation [4]:

$$N_{WP} = r_{obs}\, r_p^2 / (C_s\, D_{eff}) \qquad \text{(S5)}$$

where r_{obs} is the reaction rate per volume, r_p is the crystallite radius and taken as half (0.75 μm) of the crystallite length (1.5 μm) measured from SEM images of H-form CHA zeolites reported in our prior study [5], and C_s is the reactant concentration at the crystallite surface and taken as the bulk fluid concentration in the absence of external transport limitations. The final parameter in Equation (S5) is D_{eff}, or the effective diffusivity of each molecule within zeolite crystallites, and were estimated according to:

(i) O_2: As an order-of-magnitude estimate, D_{eff} was taken as the diffusivity of O_2 in Zeolite 5A (LTA, containing 8-membered rings) at 303 K ($1.2* 10^{-7}$ m^2 s^{-1}) [6], scaled to the reaction temperature of 473 K using Chapman-Enskog theory (2.3×10^{-7} m^2 s^{-1}):

$$D_{eff,\,T2} = D_{eff,\,T1}\,(T_2/T_1)^{3/2} \quad \text{(S6)}$$

At the most severe condition (Cu-CHA-0.37, 1 kPa O_2), $N_{WP,O2} \sim 2 \times 10^{-5} << 1$, verifying the absence of significant intracrystalline O_2 transport limitations.

(ii) NO: The diffusivity of NO in LTA was not found in the literature; thus, as an order-of-magnitude estimate, D_{eff} was taken as the diffusivity of N_2 in Zeolite 5A (LTA, containing 8-membered rings) at 303 K ($6.8* 10^{-8}$ m^2 s^{-1}) [6], scaled to the reaction temperature of 473 K using Chapman-Enskog theory (1.3×10^{-7} m^2 s^{-1}) according to Equation (S6). At the most severe condition (Cu-CHA-0.37, 60 kPa O_2), $N_{WP,NO} \sim 6 \times 10^{-3} << 1$, verifying the absence of significant intracrystalline NO transport limitations.

(iii) NH_3: D_{eff} was set equal to the reported diffusivity of saturated NH_3 in Cu-CHA at 473 K ($1.2* 10^{-9}$ m^2 s^{-1}), which was measured using quasielastic neutron scattering on a 3 wt% Cu-CHA sample (Si/Al = 17) exposed to 80 kPa NH_3 [7]. $N_{WP,NH3}$ is plotted as a function of Cu density and O_2 pressure in Figure S7. $N_{WP,\,NH3} < 1$ at all conditions, suggesting the absence of

severe intracrystalline NH_3 transport limitations. These conservative estimates of $N_{WP,\ NH3}$ become > 0.1 at higher Cu densities and O_2 pressures, however, indicating that NH_3 diffusion might affect rates measured under certain conditions.

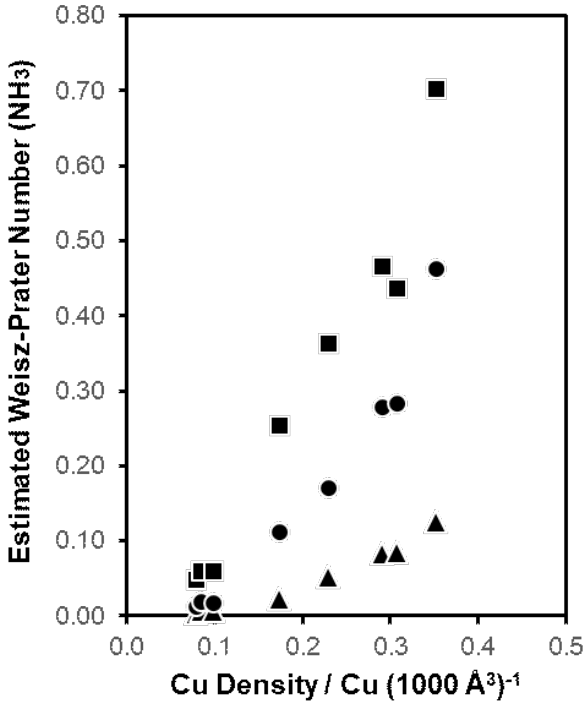

Figure S7. Estimated Weisz-Prater number for NH_3 as a function of O_2 pressure and Cu density for Cu-CHA-X samples. 1 kPa (triangles), 10 kPa (circles) and 60 kPa O_2 (squares) (reaction conditions: 0.030 kPa NO, 0.030 kPa NH_3, 1/10/60 kPa O_2, 7 kPa CO_2, 3 kPa H_2O and balance N_2 at 473 K).

Section S.5. Measurement of apparent reaction orders on Cu-CHA samples in low and high O_2 pressure limits

The data in Figure 2b (main text) are plotted in a log-log scale in Figure S8 to better visualize the quality of the fit between the measured data and the rate model (Eq. (3)).

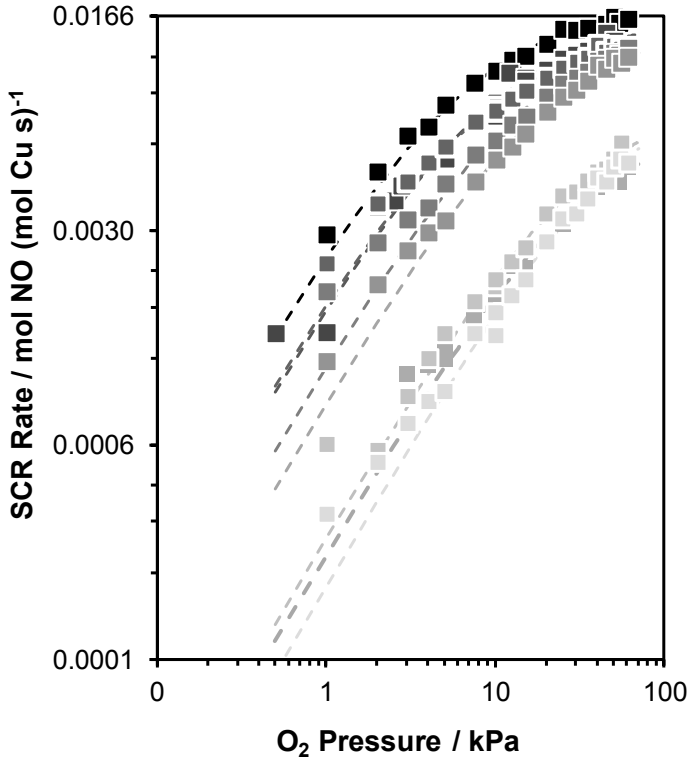

Figure S8. Steady-state SCR rates (per Cu) as a function of O_2 pressure plotted using logarithmic scales on Cu-CHA-X samples (light-to-dark shading as X increases). Dashed lines represent regression of the data to Eq. (3).

With increasing O_2 pressure (1–60 kPa), apparent NO orders increase systematically from 0.2 to 0.8, while apparent NH_3 orders remain essentially invariant near a value of -0.5 (Table S2).

Table S2. SCR kinetic parameters measured on Cu-CHA samples at 1, 10, and 60 kPa O_2.

Sample	1 kPa O_2		10 kPa O_2		60 kPa O_2	
	NO order[a]	*NH_3 order*[b]	*NO order*[a]	*NH_3 order*[b]	*NO order*[a]	*NH_3 order*[b]
Cu-CHA-0.078	-	-	0.4	-0.5	0.8	-0.5
Cu-CHA-0.17	0.3	-0.7	0.4	-0.5	0.7	-0.5
Cu-CHA-0.29	0.2	-0.5	0.6	-0.4	0.6	-0.4

[a] Other reaction conditions: 0.030 kPa NH_3, 7 kPa CO_2, 1 kPa H_2O and balance N_2 at 473 K
[b] Other reaction conditions: 0.030 kPa NO, 7 kPa CO_2, 1 kPa H_2O and balance N_2 at 473 K
Uncertainties are ± 0.1.

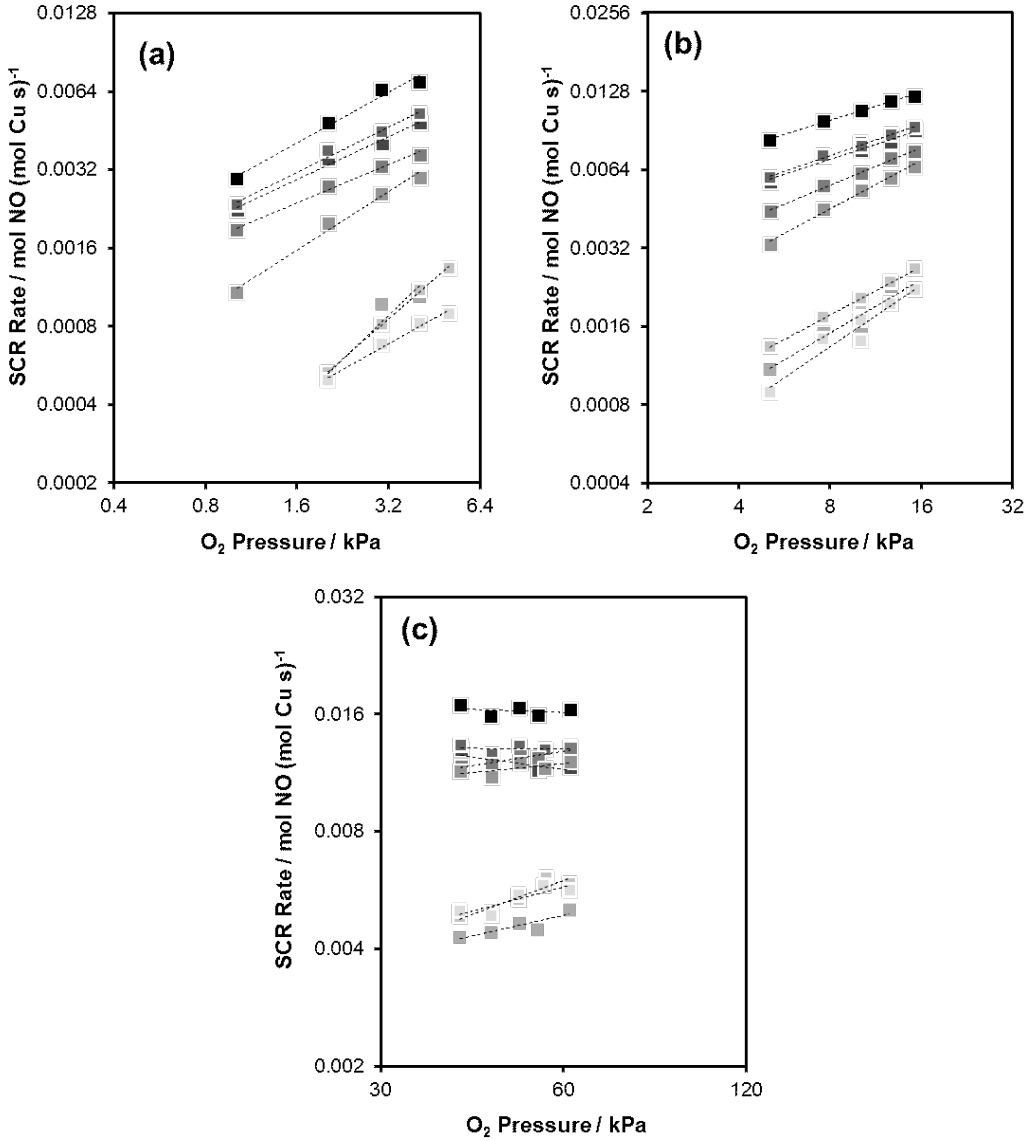

Figure S9. Steady-state SCR rate (per Cu) versus O_2 pressure on Cu-CHA-X samples (light-to-dark shading as X increases), along with best fit lines representing O_2 reaction orders, in the pressure ranges of (a) 1–4 kPa O_2 , (b) 5–15 kPa O_2, and (c) 40–60 kPa O_2. For Cu-CHA-0.78, Cu-CHA-0.084, and Cu-CHA-0.10, the O_2 reaction order in the low O_2 pressure range was instead reported from 2-5 kPa O_2 improve experimental accuracy, due to the low (~1%) NO conversion at 1 kPa O_2 for these samples.

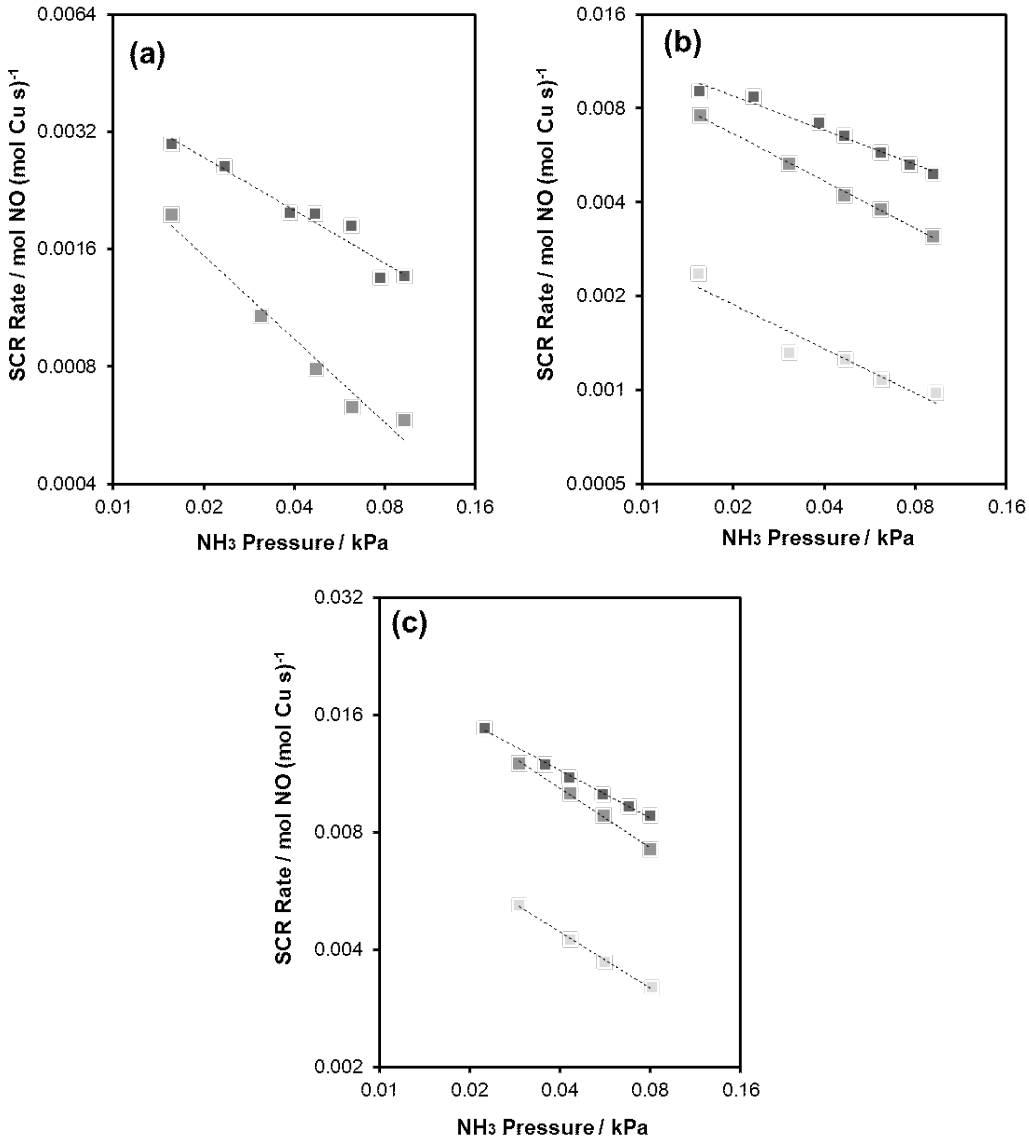

Figure S10. Steady-state SCR rate (per Cu) versus NH_3 pressure on Cu-CHA-0.078, Cu-CHA-0.17, and Cu-CHA-0.29 (light-to-dark shading as X increases), along with best fit lines representing NH_3 reaction orders, at various O_2 pressures: (a) 1 kPa O_2 (Cu-CHA-0.078 was omitted due to noisier measurements in this case), (b) 10 kPa O_2, (c) 60 kPa O_2.

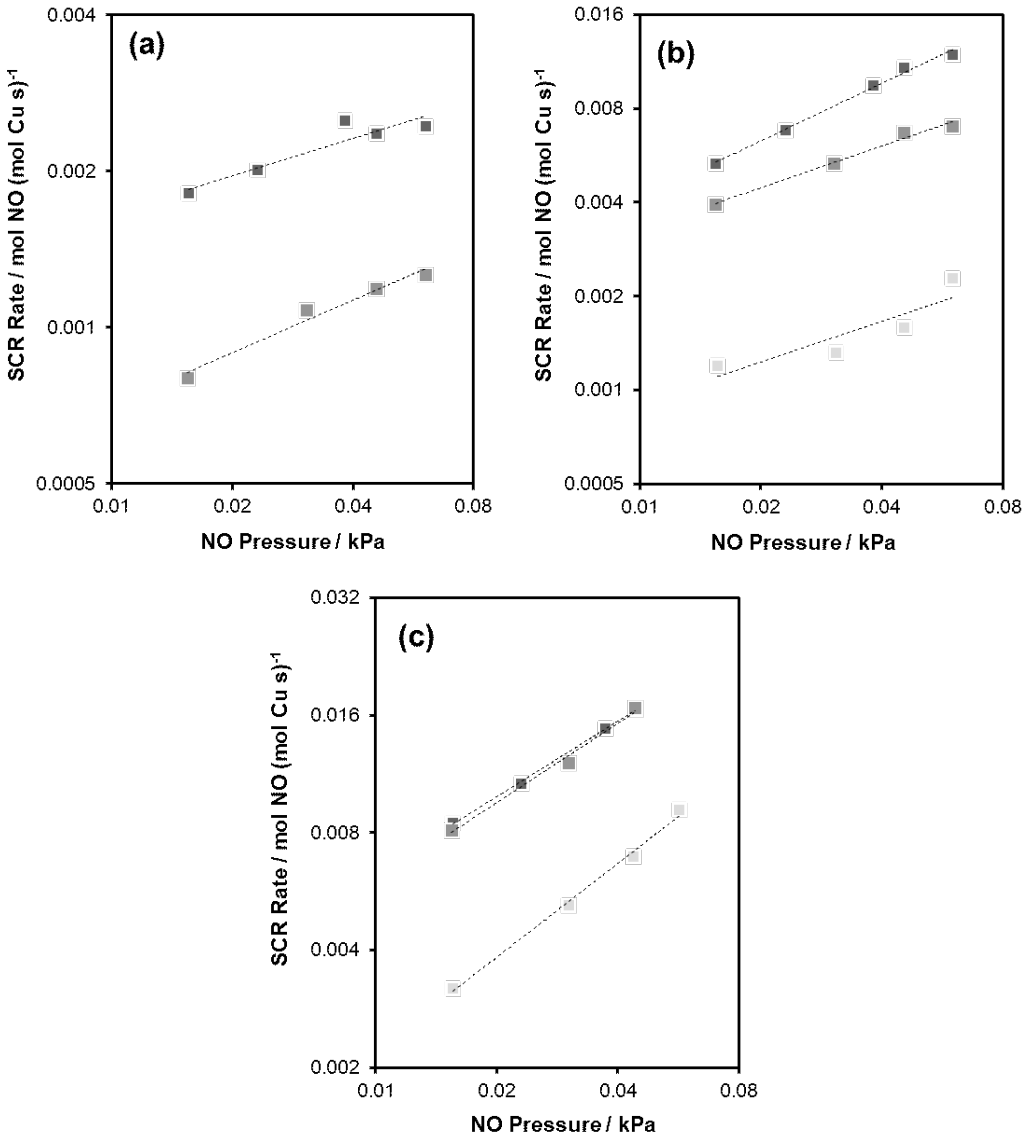

Figure S11. Steady-state SCR rate (per Cu) versus NO pressure on Cu-CHA-0.078, Cu-CHA-0.17, and Cu-CHA-0.29 (light-to-dark shading as X increases), along with best fit lines representing NO reaction orders, at various O_2 pressures: a) 1 kPa O_2 (Cu-CHA-0.078 was omitted due to noisier measurements in this case), b) 10 kPa O_2, c) 60 kPa O_2.

Section S.6. *In operando* XANES spectra of Cu-CHA-0.23 with varying O_2 pressure

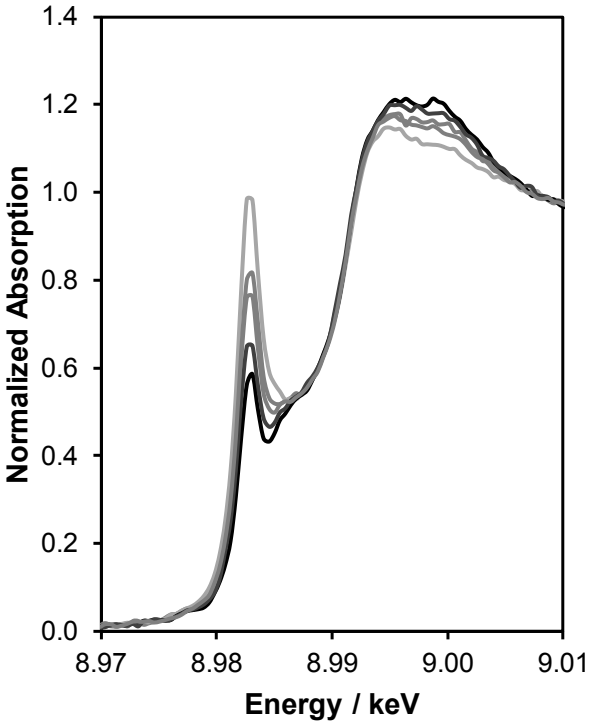

Figure S12. *In-operando* XANES spectra measured at 1 kPa O_2 5 kPa O_2, 10 kPa O_2, 30 kPa O_2, and 60 kPa O_2 (light to dark with increasing O_2 pressure). The balance gas compositions were 0.030 kPa NH_3, 0.030 kPa NO, 2 kPa H_2O, 7 kPa CO_2, and balance N_2. Linear combination fitting to Cu(I) and Cu(II) standards was performed as previously reported [1].

Section S.7. Transient O_2-assisted oxidation of pre-reduced Cu-CHA-X samples: Models to fit rate data and corresponding XANES spectra

As described in our previous study [2], the transient decrease of Cu^I with time (Fig. 4, main text) is best described by the following rate law, assuming an integral power on $[Cu^I]$:

$$\frac{d[Cu^I(t)]}{dt} = -2k_{ox}[Cu^I(t)]^2 \quad \text{(S7)}$$

In order to account for the unoxidizable Cu^I fraction (denoted as $[Cu^I(\infty)]$) observed in XANES spectra at the end of the transient O_2-assisted oxidation experiments (Figs. S13-S19), we define the concentration of Cu^I that can participate in the oxidation reaction as:

$$[Cu^I(t)]_{corr} = [Cu^I(t)] - [Cu^I(\infty)] \quad \text{(S8)}$$

$$\frac{d[Cu^I(t)]_{corr}}{dt} = -2k_{ox}[Cu^I(t)]^2_{corr} \quad \text{(S9)}$$

Since $[Cu^I(t)]_{corr}$ is the concentration of Cu^I that is oxidizable by O_2 as a function of time, Eq. (S9) can be integrated from 0 to *t*, and subsequently rearranged to yield:

$$Cu^I \text{ Fraction} = \frac{[Cu^I(t)]}{[Cu_{total}]} = \frac{1-[Cu^I(\infty)]/[Cu^I(0)]}{1+2k_{ox}([Cu^I(0)]-[Cu^I(\infty)])t} + \frac{[Cu^I(\infty)]}{[Cu^I(0)]} \quad \text{(S10)}$$

where k_{ox} and $[Cu^I(\infty)]$ are the fitted parameters. For each data series, $[Cu^I(\infty)]$ is set equal to the Cu^I fraction of the final time point, and non-linear least-squares regression was used to obtain the best-fit parameter of k_{ox} (listed in Table 3, main text).

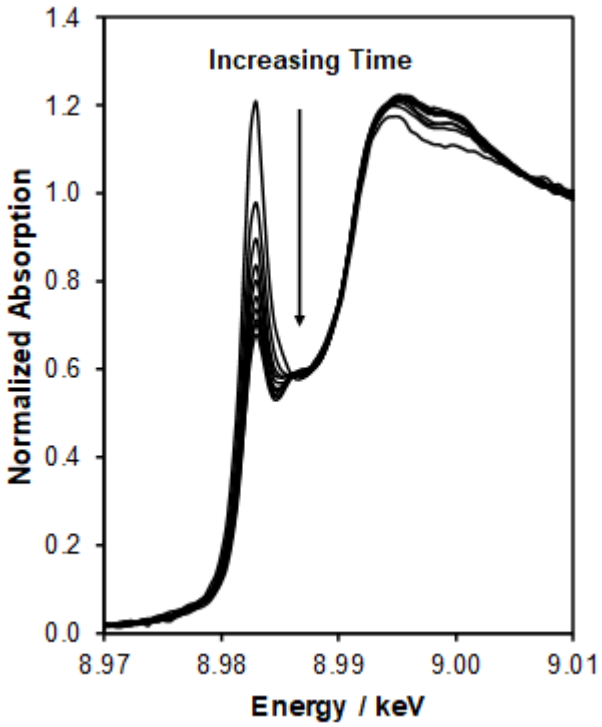

Figure S13. Time-resolved XANES spectra measured during the transient oxidation of Cu-CHA-0.078 (473 K, 10 kPa O_2) after treatment in 0.030 kPa NO and 0.030 kPa NH_3 at 473 K. A total of 40 spectra were collected in 20 second intervals. The first 10 spectra are plotted for clarity.

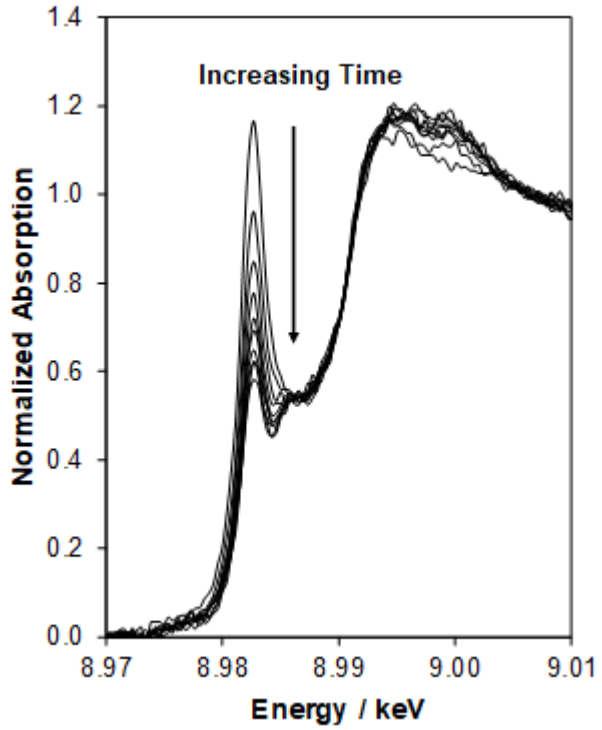

Figure S14. Time-resolved XANES spectra measured during the transient oxidation of Cu-CHA-0.10 (473 K, 10 kPa O_2) after treatment in 0.030 kPa NO and 0.030 kPa NH_3 at 473 K. A total of 40 spectra were collected in 20 second intervals. The first 10 spectra are plotted for clarity.

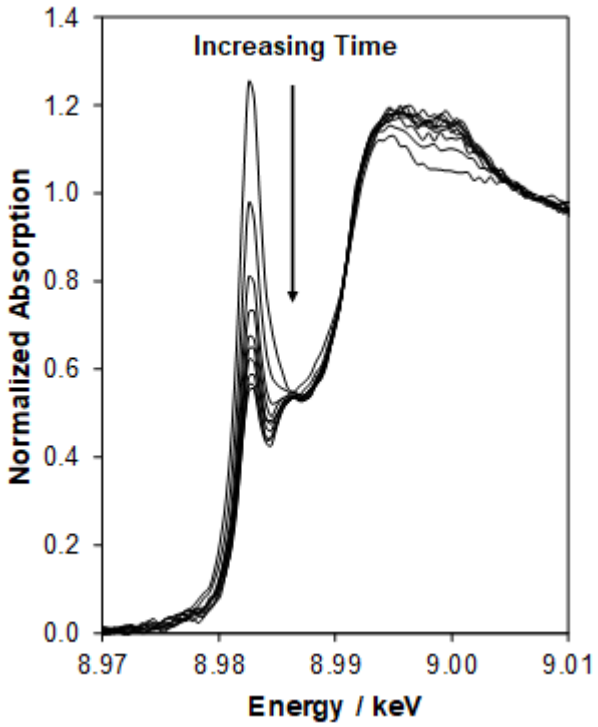

Figure S15. Time-resolved XANES spectra measured during the transient oxidation of Cu-CHA-0.17 (473 K, 10 kPa O_2) after treatment in 0.030 kPa NO and 0.030 kPa NH_3 at 473 K. A total of 40 spectra were collected in 14.5 second intervals. The first 10 spectra are plotted for clarity.

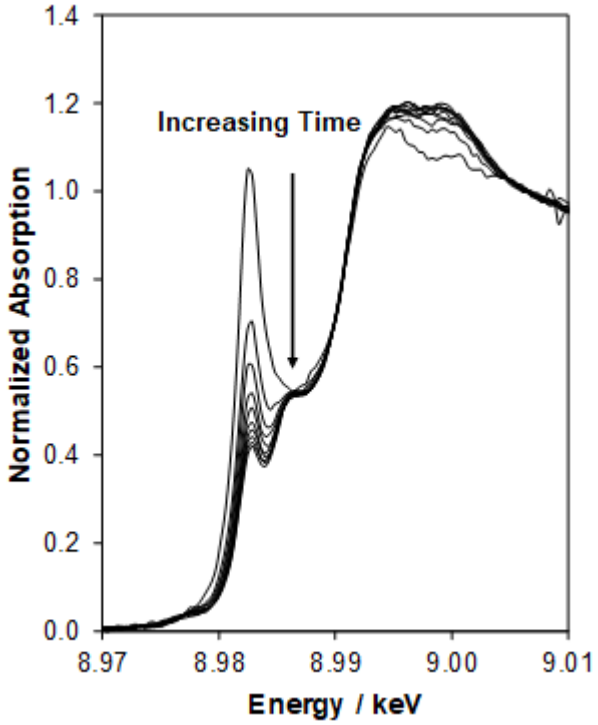

Figure S16. Time-resolved XANES spectra measured during the transient oxidation of Cu-CHA-0.23 (473 K, 10 kPa O_2) after treatment in 0.030 kPa NO and 0.030 kPa NH_3 at 473 K. A total of 30 spectra were collected in 21.5 second intervals. The first 10 spectra are plotted for clarity.

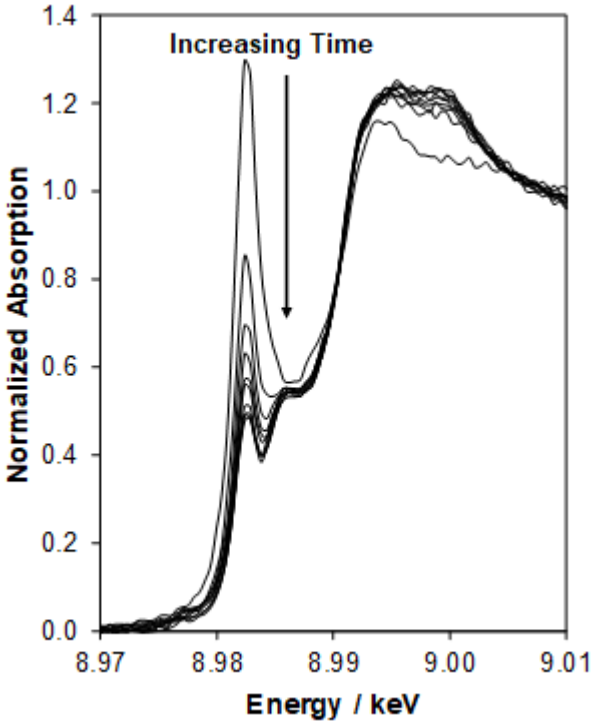

Figure S17. Time-resolved XANES spectra measured during the transient oxidation of Cu-CHA-0.29 (473 K, 10 kPa O_2) after treatment in 0.030 kPa NO and 0.030 kPa NH_3 at 473 K. A total of 39 spectra were collected in 14.5 second intervals. The first 10 spectra are plotted for clarity.

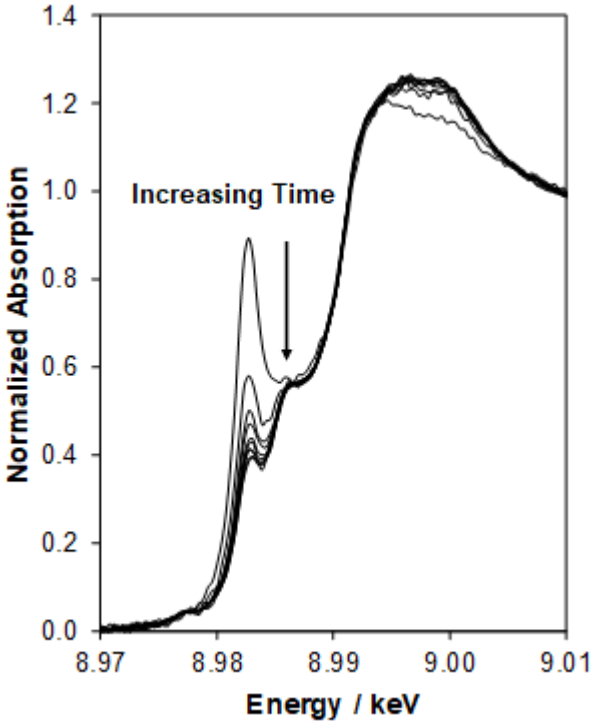

Figure S18. Time resolved XANES spectra measured during the transient oxidation of Cu-CHA-0.31 (473 K, 10 kPa O_2) after treatment in 0.030 kPa NO and 0.030 kPa NH_3 at 473 K. A total of 32 spectra were collected in 21.5 second intervals. The first 10 spectra are plotted for clarity.

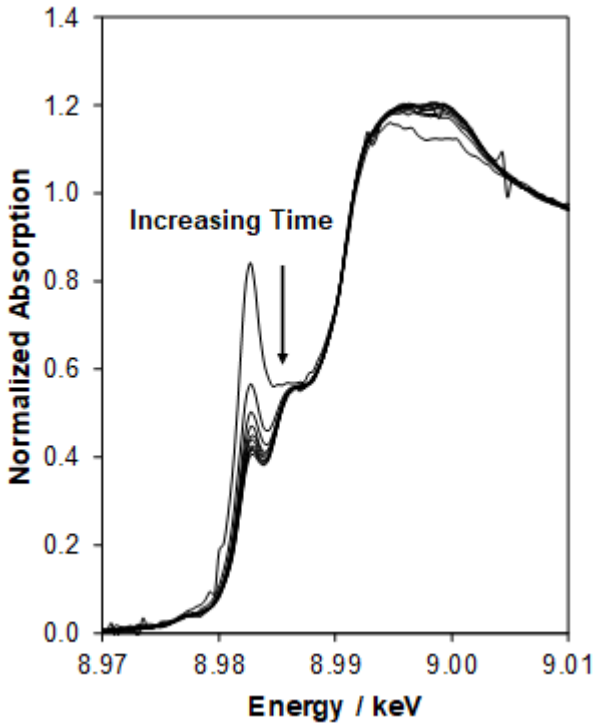

Figure S19. Time-resolved XANES spectra measured during the transient oxidation of Cu-CHA-0.35 (473 K, 10 kPa O_2) after treatment in 0.030 kPa NO and 0.030 kPa NH_3 at 473 K. A total of 30 spectra were collected in 21.5 second intervals. The first 10 spectra are plotted for clarity.

Section S.8. Transient NO+NH_3-assisted reduction of oxidized Cu-CHA-X samples: Models to fit rate data and corresponding XANES spectra

The transient decrease in Cu^{II} during reduction in NO and NH_3 can be described by a rate law that is first-order in Cu:

$$\frac{d[Cu^{II}(t)]}{dt} = -k_{red}[Cu^{II}(t)] \quad \text{(S11)}$$

In some samples studied, XANES spectra at the end of the transient NO+NH_3-assisted reduction experiments (Figs. S20-S24) showed small percentages (≤10%) of Cu^{II} that were not reduced, although we note that these values are within the uncertainty of the linear combination XANES fitting procedure. For the purposes of modeling the data in Figure 6 (main text), we define the fraction of Cu that are able to reduce as:

$$[Cu^{II}(t)]_{corr} = [Cu^{II}(t)] - [Cu^{II}(\infty)] \quad \text{(S12)}$$

$$\frac{d[Cu^{II}(t)]_{corr}}{dt} = -k_{red}[Cu^{II}(t)]_{corr} \quad \text{(S13)}$$

Integration of Eq. (S13) yields the following expression:

$$Cu^{II}\ \text{Fraction} = \frac{[Cu^{II}(t)]}{[Cu_{total}]} = \frac{[Cu_0^{II}]-[Cu_\infty^{II}]}{[Cu_{total}]} e^{-k_{red}t} + \frac{[Cu_\infty^{II}]}{[Cu_{total}]} \quad \text{(S14)}$$

Where k_{red} and $[Cu^{II}(\infty)]$ are fitted parameters. For each data series, $[Cu^{II}(\infty)]$ was set equal to the Cu^{II} fraction of the final time point, and non-linear least-squares regression was used to obtain the best-fit parameter of k_{red} (listed in Table 3, main text).

The transient reduction rate constants measured here were compared to a similar experiment reported in the literature by Liu et al. [8] using the following approximations. First, their reported initial rate of NO and NH_3 reduction (1.7 mmol NO g^{-1} h^{-1} at 0.05 kPa NO and 423 K) was converted to the units of our reduction rate constant:

$$1.7\ \frac{\text{mmol NO}}{\text{g h}} \times \frac{1\ \text{g cat}}{0.02\ \text{g Cu}} \times \frac{63.546\ \text{g Cu}}{\text{mol}} \times \frac{1\ \text{h}}{3600\ \text{s}} \times \frac{1\ \text{mol}}{1000\ \text{mmol}} = 0.0015\ \frac{\text{mol NO}}{\text{mol Cu s}} \quad \text{(S15)}$$

Next, the Arrhenius equation was applied to estimate this rate at 473 K, assuming an activation energy of 70 kJ/mol, which is consistent with reported apparent activation energies for low-temperature SCR in the reduction-limited regime [2,9]:

$$r_{NO,473K} = r_{NO,423K} \times e^{\frac{Ea}{R}\left[\frac{1}{423}-\frac{1}{473}\right]} = 0.012\ \frac{mol\ NO}{mol\ Cu\ s} \qquad \text{(S16)}$$

Finally, it was assumed that transient NO and NH_3 reduction is first-order in NO, and this rate was scaled by the ratio of NO pressures in the two experiments (3/5) to achieve the final estimate for the rate constant of 0.007 s^{-1}, which is quantitatively consistent with our measurement.

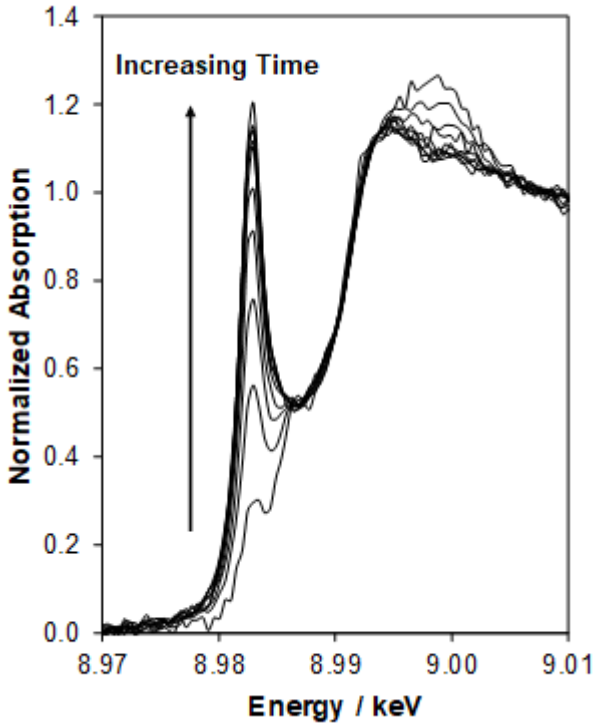

Figure S20. Time-resolved XANES spectra measured during the transient reduction of Cu-CHA-0.078 (473 K, 0.030 kPa NH_3, 0.030 kPa NO) after treatment in 20 kPa O_2 at 673 K. A total of 30 spectra were collected in 16.5 second intervals. The first 10 spectra are plotted for clarity.

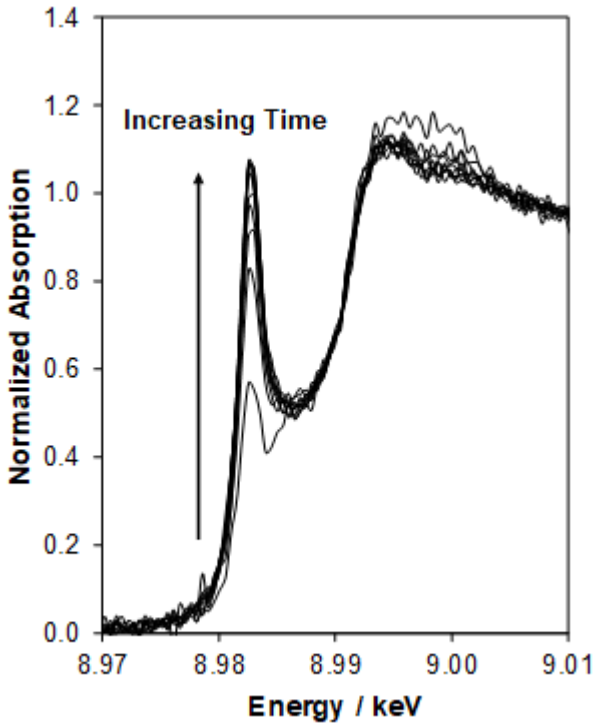

Figure S21. Time-resolved XANES spectra measured during the transient reduction of Cu-CHA-0.084 (473 K, 0.030 kPa NH_3, 0.030 kPa NO) after treatment in 20 kPa O_2 at 673 K. A total of 37 spectra were collected in 22.5 second intervals. The first 10 spectra are plotted for clarity.

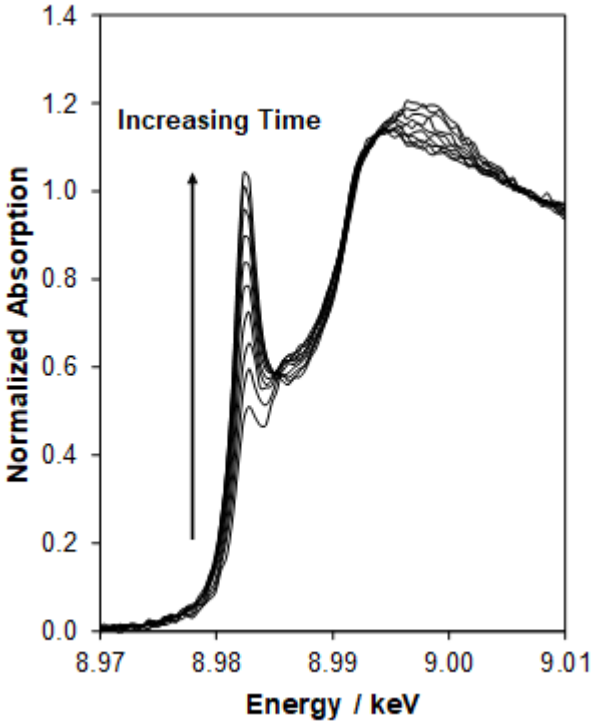

Figure S22. Time-resolved XANES spectra measured during the transient reduction of Cu-CHA-0.17 (473 K, 0.030 kPa NH_3, 0.030 kPa NO) after treatment in 20 kPa O_2 at 673 K. A total of 40 spectra were collected in 14.5 second intervals. The first 10 spectra are plotted for clarity.

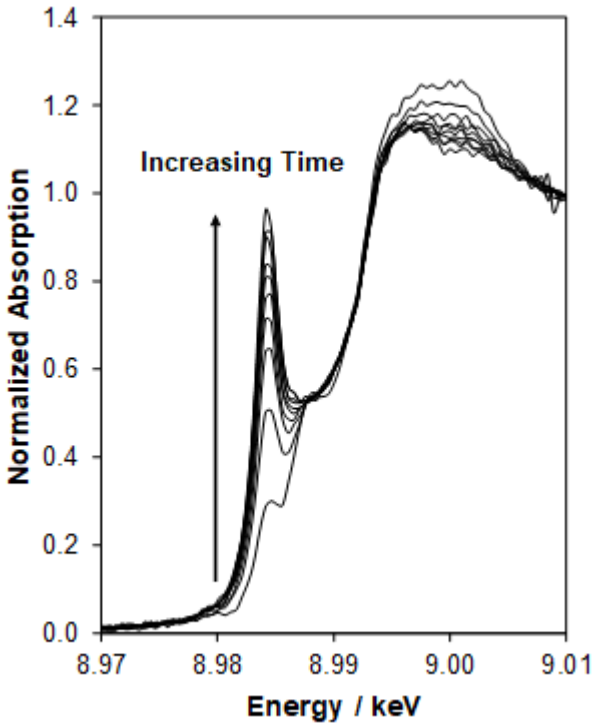

Figure S23. Time-resolved XANES spectra measured during the transient reduction of Cu-CHA-0.23 (473 K, 0.030 kPa NH_3, 0.030 kPa NO) after treatment in 20 kPa O_2 at 673 K. A total of 54 spectra were collected in 22.5 second intervals. The first 10 spectra are plotted for clarity.

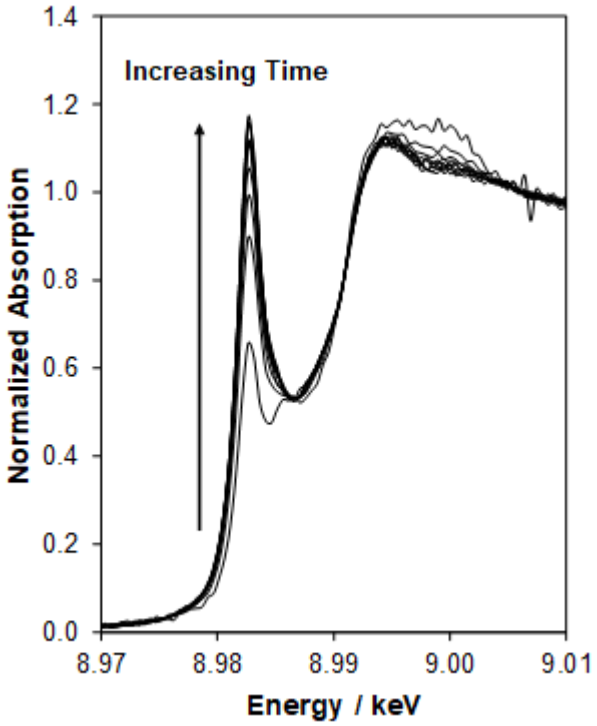

Figure S24. Time resolved XANES spectra measured during the transient reduction of Cu-CHA-0.35 (473 K, 0.030 kPa NH_3, 0.030 kPa NO) after treatment in 20 kPa O_2 at 673 K. A total of 21 spectra were collected in 22.5 second intervals. The first 10 spectra are plotted for clarity.

Section S.9. References

[1] C. Paolucci, A.A. Parekh, I. Khurana, J.R. Di Iorio, H. Li, J.D. Albarracin Caballero, A.J. Shih, T. Anggara, W.N. Delgass, J.T. Miller, F.H. Ribeiro, R. Gounder, W.F. Schneider, Catalysis in a Cage: Condition-Dependent Speciation and Dynamics of Exchanged Cu Cations in SSZ-13 Zeolites., J. Am. Chem. Soc. 138 (2016) 6028–48. https://doi.org/10.1021/jacs.6b02651.

[2] C. Paolucci, I. Khurana, A.A. Parekh, S. Li, A.J. Shih, H. Li, J.R.D. Iorio, J.D. Albarracin-Caballero, A. Yezerets, J.T. Miller, W.N. Delgass, F.H. Ribeiro, W.F. Schneider, R. Gounder, Dynamic multinuclear sites formed by mobilized copper ions in NOx selective catalytic reduction, Science. 357 (2017) 898–903. https://doi.org/10.1126/science.aan5630.

[3] H. Tsukahara, T. Ishida, M. Mayumi, Gas-Phase Oxidation of Nitric Oxide: Chemical Kinetics and Rate Constant, Nitric Oxide. 3 (1999) 191–198. https://doi.org/10.1006/niox.1999.0232.

[4] P.B. Weisz, C.D. Prater, Interpretation of Measurements in Experimental Catalysis, in: W.G. Frankenburg, V.I. Komarewsky, E.K. Rideal (Eds.), Adv. Catal., Academic Press, 1954: pp. 143–196. https://doi.org/10.1016/S0360-0564(08)60390-9.

[5] J.R. Di Iorio, C.T. Nimlos, R. Gounder, Introducing Catalytic Diversity into Single-Site Chabazite Zeolites of Fixed Composition via Synthetic Control of Active Site Proximity, ACS Catal. 7 (2017) 6663–6674. https://doi.org/10.1021/acscatal.7b01273.

[6] D.M. Ruthven, Z. Xu, Diffusion of oxygen and nitrogen in 5A zeolite crystals and commercial 5A pellets, Chem. Eng. Sci. 48 (1993) 3307–3312. https://doi.org/10.1016/0009-2509(93)80214-B.

[7] A.J. O'Malley, I. Hitchcock, M. Sarwar, I.P. Silverwood, S. Hindocha, C.R.A. Catlow, A.P.E. York, P.J. Collier, Ammonia mobility in chabazite: insight into the diffusion component of the NH3-SCR process, Phys. Chem. Chem. Phys. 18 (2016) 17159–17168. https://doi.org/10.1039/C6CP01160H.

[8] C. Liu, H. Kubota, T. Amada, K. Kon, T. Toyao, Z. Maeno, K. Ueda, J. Ohyama, A. Satsuma, T. Tanigawa, N. Tsunoji, T. Sano, K. Shimizu, In Situ Spectroscopic Studies on the Redox Cycle of NH3–SCR over Cu-CHA Zeolites, ChemCatChem. (n.d.). https://doi.org/10.1002/cctc.202000024.

[9] F. Gao, D. Mei, Y. Wang, J. Szanyi, C.H.F. Peden, Selective Catalytic Reduction over Cu/SSZ-13: Linking Homo- and Heterogeneous Catalysis, J. Am. Chem. Soc. 139 (2017) 4935–4942. https://doi.org/10.1021/jacs.7b01128.